Defying Limits: Electron Interactions with Atmospheric Species

By

Beverly (Ru) Feng

A Dissertation Submitted to the Faculty of the

DEPARTMENT OF CHEMISTRY AND BIOCHEMISTRY

In Partial Fulfillment of the Requirements

For the Degree of

DOCTOR OF PHILOSOPHY

IN PHYSICAL CHEMISTRY

In the Graduate College of

THE UNIVERSITY OF ARIZONA

2023

THE UNIVERSITY OF ARIZONA
GRADUATE COLLEGE

As members of the Dissertation Committee, we certify that we have read the dissertation prepared by: *Beverly Feng*, titled: *Defying Limits: Electron Interactions with Atmospheric Species*

and recommend that it be accepted as fulfilling the dissertation requirement for the Degree of Doctor of Philosophy.

_____ Date: _____
Dr. Andrei Sanov

_____ Date: _____
Dr. Michael Brown

_____ Date: _____
Dr. Dennis Lichtenberger

_____ Date: _____
Dr. Steve Schwartz

Final approval and acceptance of this dissertation is contingent upon the candidate's submission of the final copies of the dissertation to the Graduate College.

I hereby certify that I have read this dissertation prepared under my direction and recommend that it be accepted as fulfilling the dissertation requirement.

_____ Date: _____
Dr. Andrei Sanov
Dissertation Committee Chair
Department of Chemistry and Biochemistry

Acknowledgements

My time and progress at the University of Arizona would not have been made easier without the guidance, help, and support that I have received from various colleagues, faculties, and people.

I want to first thank my research advisor Professor Andrei Sanov, who supported me throughout my whole graduate career. He never doubted my capabilities as a researcher, teaching assistant, or as a person. He was always available whenever I needed help in experiments, computations, or teaching. If I was too afraid of opening an ampule of a new chemical I never used, he would, without hesitation, do it instead. He would put health and safety first in front of anything else, which made me a better person and researcher. When the lab dwindled down, I went to Professor Sanov for confirmation and verification in my procedures. He was never bothered by the countless times I knocked on the door to make sure I was doing things correctly. Due to Professor Sanov, I have become a better scientist, researcher, teacher, and person. I would not want any other advisor than him.

The help and support of Christopher Blackstone was endless. He was a senior graduate student when I first joined the lab. He helped trained me on the instrument and the research done in this group. He not only motivated me through difficult situations, but also challenged me to solve problems alone. He believed in me more than I believed in myself. Also, he taught me the art of walking to the undergraduate academic advising center for candies when stressed. Through Chris, I also learned that in graduate school, a work-life balance was a possibility with proper time management. This was an important skill to learn, especially in graduate school. I was able to juggle between research, teaching, and my hobbies. This allowed me to destress and evidently become a better researcher. Furthermore, Adam Wallace and Yerbolat Dauletyarov were older

graduate students in the lab as well. They have helped me with understanding the research in the group as well as instrumentations and computational calculations. I was able to ask for advice on various subjects and ideas with them.

I want to acknowledge Lori Boyd for helping with my time at the university. I want to thank the research support facilities here at the University of Arizona. Special thank you to Lee Macomber, Paul Lee, Kevin Bao, Justan Klaus, and Charles Amling. They have all helped me with my instrumentation and research problems. Without their support, I would not have a working instrument or moved forward with my research.

I want to thank my committee members Dr. Michael Brown, Dr. Dennis Lichtenberger, and Dr. Steve Schwartz. Thank you for taking the time to help and guiding me through my graduate career. Everyone was constantly motivating and supporting me through my time here. I also want to thank you for reading through and evaluating my work for this dissertation and Ph.D. Due to your help, I have become a better scientist.

Moreover, I want to acknowledge my mom and brother with their endless support during my time here. I also want to thank my partner, Levi Newton, for continuing to cheer me on, believe in me, and support me. Lastly of course, my spoiled dog, Luna, has helped me by decreasing my stress through various ways.

Dedications

To my mom and dad, brother, grandmother,

and my partner, Levi:

Thank you all for the endless love and support.

Table of Contents

Table of Contents - continued

Table of Contents - continued

List of Figures

List of Tables

Abstract

This dissertation encompasses the idea of defying limitations or common generalizations- the abnormal methods that are needed and used in these discussed experiments. Photoelectron imaging spectroscopy is used to study the electronic properties and structures of negative ions. The following anions are studied: sulfur monoxide anion (SO^-), phenide anion (Ph^-), and phenide-water clusters (Ph^-H_2O and $Ph^-(H_2O)_2$). The common assumption used is that the photoejected electron has little to no interaction with the neutral species. The observations and understanding of hydration shift and stabilizations in the photoelectron spectroscopy community reference from anions at the ground state and not for thermally excited polyatomic ensembles. *Ab initio* calculations become limited in this sense, such that new methods are required to fully analyze the congested experimental spectra. Microhydration interactions determines the upper bound limit temperature of stable clusters or the characteristic solvation temperature.

The photoelectron angular distributions (PADs) of SO^- is studied and compared through experimental and computational methods. The departing photoelectron interacts with the neutral residue of SO due to significant dipole moment, making common *ab initio* computational methods that are used for photoelectron anisotropy parameters limited. Different methods (point dipole-field and multi-center) were used instead to understand the exit-channel interactions of SO for the $X\,^3\Sigma^-$ state and $a\,^1\Delta$ state. The point dipole-field model with $D > 0.6$ a.u. (D = dipole moment) and the multi-center model with $Z_S = 0.10 – 0.15$ (partial charge on the sulfur atom) were consistent with the experimental PADs data. The research on SO^- advances the dipole-field model by introducing detachment from a π^*orbital.

Analyzing the data of hot species vs. cold species require different methods that are not as straight forward, which is seen in both phenide and phenide-water clusters. Calculating using only

the state-specific approach would result in millions of years to converge; therefore, statistical methods (e.g., energy conservation model) were used to analyze the congested photoelectron energy spectrum for hot phenide. The Franck-Condon (FC) factors of ground cold phenide (0 K) was used as a reference for the statistical models. The estimated experimental temperature of phenide was found to be 700 K. The temperature of phenide-water cluster was 560 K, which was determined by the characteristic solvation temperature (CST). The CST is an intrinsic property of the clusters and is determined by the microsolvation interactions and not by the electron source (e.g., electron cannon) temperature.

Furthermore, experiments have been done on O_2^- Benzoxazole with calculations still in the process. This project will add more information on how different solvents (e.g., benzoxazole) affect the oxygen anion. This also continues the research of how the departing electron cannot be assumed as negligible. Future experiments on S_2^- solvated with other species will hopefully be performed to peer into the affect of changing the anion core between O_2^- and S_2^-. Lastly, hot ions will still be investigated as this is a relatively new topic in the Sanov lab.

Chapter 1: Introduction

1.1 Defying Approximation Limits

Trends and patterns occur in our everyday life, from making up our established daily routine to explaining the obtained research data. Often, mathematically speaking, trends and patterns in chemistry can be summed up or generalized according to approximations. These general approximations and limits help guide and explain the wonders of science, either through experiments or computational calculations. However, these general approximations are by their very definition limiting the scope of our understanding of nature. Meaning that they do not explain and account for *everything*.

In this case, "Defying Limits: Electron Interactions with Atmospheric Species" is presented based on these studied atmospheric species: the SO diradical, phenide, and phenide clusters. In SO^-, the general approximation of a departing electron having little to no interaction with the neutral residue cannot be used as a model for this study. This is due to the neutral residue of sulfur monoxide possessing a significant dipole moment of 1.45 Debye. Sulfur monoxide anion is discussed in Chapter 3. Furthermore, hot ions are an example of how classical harmonic limits have limitations. Details about hot ions and solvated hot ions will be discussed later in Chapters 4 and 5, respectively.

1.2 Importance of Atmospheric Species

Research on the atmosphere provides insight into how molecular interactions occur in changing environments. Atmospheric chemistry encompasses complex systems of naturally occurring and man-made reaction cycles, resulting in the production of radical intermediates,

solvated clusters, and chemically important products that affect the planets and interstellar space. Radical intermediates are often unstable and difficult to study but play an important role in the changing climate on Earth and the vast interstellar space. Solvated clusters help understand how aerosols are affecting the cloud condensation nuclei and cloud droplets in Earth's atmosphere.[1] These species are important to study as they tell how they are affected or affect other molecules or ions around them.[2]

Furthermore, hot ions are important to understand due to the interactions they may have in the atmosphere, such as aerosol formations. These hot ions may be formed due to jet engine exhausts or other various combustion methods. Little has been studied about hot ions in the photoelectron imaging spectroscopy community due to the instability and the different instrumentation set-up of these ion formations.

Possible atmospheric species that were focused on, listed in this dissertation, as mentioned earlier: SO^- and hot ions (phenide and phenide clusters). The importance of SO^- and hot ions is further discussed in Chapter 3 and Chapter 4, respectively. We mainly focused on the experimental and computational photoelectron angular distributions (PAD) of SO^-, the photoelectron spectroscopy and statistical analysis of hot phenide, and understanding the microhydrations on hot phenide clusters. The fundamental properties of these negative species are understood to peer into the physical chemistry aspect of electrons *via* negative ions photoelectron imaging spectroscopy, such as the electronic properties and the molecular orbitals.

1.3 Photoelectron Imaging Spectroscopy of Anions

Photoelectron imaging spectroscopy is used to observe and understand the electronic structures of the studied species, providing information about the kinetic energy of the

photodetached electron and the molecular orbitals of the neutral from the photoelectron image obtained. The details of the instrumentation and experimental design are discussed in Chapter 2. The specifics of each experiment for the earlier listed projects can be found in their respective chapters mentioned earlier. This spectroscopy method takes advantage of the well-known photoelectric effect described by the equation,

$$\mathrm{eKE} = h\nu - \mathrm{eBE} \tag{1.1}$$

where the kinetic energy of the photoemitted electrons (eKE) is determined by the energy of the absorbed photon ($h\nu$) minus the electron binding energy (eBE). A light source, such as a laser, is used to photoeject an electron from the anion.

A photoelectron image is obtained after hundreds of thousands of iterations of photoejected electrons hitting the detector (discussed in Section 2.5 of Chapter 2). The analyzed image gives the photoelectron energy spectrum. The electronic and vibrational peaks on this spectrum comes from the Franck-Condon (FC) principle. In our case, the Franck-Condon principle describes the intensity of a vibrational peak from an allowed electronic transition between the anion (initial) and neutral (final) state from the absorption of a photon, shown in Equation 1.2,

$$\langle \psi^*_{\mathrm{final}} | \psi_{\mathrm{initial}} \rangle = \langle \psi^*_{\mathrm{f,nucleus}} | \psi_{\mathrm{i,nucleus}} \rangle \langle \psi^*_{\mathrm{f,electron}} | \hat{\mu} | \psi_{\mathrm{i,electron}} \rangle \tag{1.2}$$

where $\hat{\mu}$ is the dipole operator that is dependent only on the electronic components. This principle is based off the Born-Oppenheimer Approximation, where the nuclei are fixed relative to their fast-moving electrons. It is assumed that the neutral molecule has the same geometry as the anion when the electron is photoejected from the anion, giving the vertical detachment energy (VDE).

The VDE roughly corresponds to the most intense peak in the energy spectrum, which reflects the greatest overlap between the vibrational wavefunctions of the ground state of the anion

and the ground state of the neutral. This differs the diabatic detachment energy or electron affinity, where the zero vibrational level of the ground electronic state of the anion is connected to the zero vibrational level of the ground electronic state of the neutral. In general, VDE calculations have helped compare experimental data with computational data; however, in some cases, the VDE calculations can differ from the experimental data greatly due to specific circumstances that is explained in the projects in this dissertation. Furthermore, the photoelectron angular distributions (PADs) can be calculated from the photoelectron energy spectra.

1.4 The Photoelectron Angular Distributions

PADs can be determined by integrating over the radial of a particular angle on the image. These integrations are repeated in 0.5º increments to give integrated values at each angle. The PAD usually reflects the character of the parent orbital. For atomic anions, it follows the selection rule of $\Delta l = \pm 1$, where l is the orbital angular momentum quantum number. For molecular species, the selection rules are more complicated as described elsewhere.[3] PADs for one-photon photodetachment transitions are uniquely described by the photoelectron anisotropy parameter β, according to the equation:[4-6]

$$I(\theta) = a[1 + \beta P_2(\cos\theta)] \tag{1.3}$$

where $I(\theta)$ is the electron emission intensity at angle θ, a is the detachment cross-section, $P_2(\cos\theta)$ is the second-order Legendre polynomial, and β is the unitless anisotropy parameter that ranges from 2 to –1. The two limiting cases of anisotropic transitions to consider are parallel and perpendicular transitions described by $\beta = 2$ and $\beta = -1$, respectively. The parameters are parallel or perpendicular to the laser polarization vector. When $\beta = 0$, the transition is isotropic and anisotropic if $\beta \neq 0$. The β parameter is generally dependent on the photoelectron kinetic

energy. For example, when $\beta = 2$, this corresponds to a pure *p* wave limit observed in *s* orbital photodetachment. In *p* orbital photodetachment, the emitted electron is described by interference of *s* and *d* partial waves. Their relative amplitudes vary with eKE, resulting in an eKE-dependence of PADs and therefore, β.

The Cooper-Zare central-potential formula for an atomic transition was generalized by Cooper and Zare and derivation by Bethe:[4-5, 7]

$$\beta_l = \frac{l(l-1)\chi_{l,l-1}^2 + (l+1)(l+2)\chi_{l,l+1}^2 - 6l(l+1)\chi_{l,l+1}\chi_{l,l-1}\cos\delta_{l+1,l-1}}{(2l+1)[l\chi_{l,l-1}^2 + (l+1)\chi_{l,l+1}^2]} \quad (1.4)$$

where $\chi_{l,l\pm1}$ are the magnitudes of the radial transition dipole matrix element of $l \pm 1$ (l = angular momentum quantum number) partial waves from the parent atomic orbital and $\delta_{l+1,l-1}$ is the phase shift between the interactions of the residual neutral or ion. This can be applied to a few molecular cases. The Sanov group has derived a general equation (Equation 1.5) to deal with molecular cases with mixed orbitals:[8]

$$\beta = \frac{\sum_l \gamma_l\,[l(l-1)\chi_{l,l-1}^2 + (l+1)(l+2)\chi_{l,l+1}^2 - 6l(l-1)\chi_{l,l-1}\chi_{l,l+1}\cos\delta_{l+1,l-1}]/(2l+1)}{\sum_l \gamma_l[l\chi_{l,l-1}^2 + (l+1)\chi_{l,l+1}^2]} \quad (1.5)$$

this is under the assumption that the neutral molecule has little to no significant dipole moment. For a detachment from a mixed-character orbital described as $|\psi_{\mathrm{pd}}\rangle = \sqrt{1-\gamma_{\mathrm{d}}}|\mathrm{p}\rangle + \sqrt{\gamma_{\mathrm{d}}}|\mathrm{d}\rangle$, where γ_{d} is the fractional d-character ($0 \leq \delta_{\mathrm{d}} \leq 1$), then the $\beta(\varepsilon)$:[8]

$$\beta = \frac{(1-\gamma_{\mathrm{d}})B_2\varepsilon\left(2A_1^2\varepsilon^2 - 4A_1\varepsilon\cos\delta_{2,0}\right) + \gamma_{\mathrm{d}}A_1^2\varepsilon^2(2 + 12A_2^2\varepsilon^2 - 36A_2\varepsilon\cos\delta_{3,1})]/5}{(1-\gamma_{\mathrm{d}})B_2\varepsilon(1+2A_1^2\varepsilon^2) + \gamma_{\mathrm{d}}A_1^2\varepsilon^2(2+3A_2^2\varepsilon^2)} \quad (1.6)$$

The A_1, A_2, and B_2 are known as the generalized Hanstorp coefficients that describes the scaling of p → d over p → s (for A_1), d → f over d → p (for A_2), and p → d over d → p (for B_2).[9] While this equation can be used to express some models (e.g., O_2^-), this assumption is broken when cases

like CN^- and SO^- were observed and experimented. Modeling the PADs of SO^- is further discussed in Chapter 3 and elsewhere.

1.5 Dissertation Outline

In this dissertation, Chapter 2 discusses the specifics of the instrument, including dimensions, voltages, and other important aspects. The experimental parameters are discussed as well. Furthermore, the differences between the electron gun vs. the electron cannon is mentioned with the possibility of temperature control using the electron gun. Most experiments discussed in this dissertation use the electron cannon set-up.

Chapter 3 discusses how photoelectron angular distribution cannot be modeled using the common Cooper-Zare model because of dipole interaction with the leaving electron on the neutral residue. Chapter 4 introduces the idea of hot ions using phenide as an example. It is shown that with the help of Franck-Condon calculations and statistical analysis that temperature of ions can be approximated. Chapter 5 further examines hot ions, but now studies the interactions with hot ions and solvents or the microhydration interactions. This is seen through hot phenide clusters. Chapter 6 is the summarized experiments and future directions as well as future experiments. This dissertation goes more into the important and significant findings of each experiment and is not focused on providing all the in-depth details that can be found in the respective published papers.

Chapter 2: Instrumentation and Experimental Design

This section describes the specifications of the instrumentation and experimental methods. An in-depth detailed description and specification of the instrumentation has been given elsewhere.[10-11] Here we provide a brief outline. The custom-built anion photoelectron imaging spectroscopy instrument is comprised of three major sections: the ion source chamber, the time-of-flight (TOF), and the detection region as shown in Figure 2.1. The source chamber is connected to the TOF region by a 4 mm aperture, located at the entrance of the acceleration stack. The TOF is connected to the detection region by a 4" pneumatic gate valve and a 1-inch aperture. The source chamber, TOF, and detection region all have different pressures described later in this chapter. In addition, this chapter also covers the lasers used and velocity-map imaging (VMI) apparatus located in the detection region in Sections 2.4 and 2.5, respectively. The imaging collecting process used is discussed in Section 2.5. Wrapping up the different types of ion formations produced in the source chamber are discussed in Section 2.6.

2.1 Vacuum Hardware Specification

The source chamber is kept at a base pressure of $1–7\times10^{-5}$ Torr during experiments and maintained at $3–6\times10^{-6}$ Torr otherwise. A pneumatic gate valve (Vacuum Research Ltd., 10-inch ASA flanges) separates the 10-inch diffusion pump (DP; Varian VHS-10; pumping speed: 3650 L/s) from the source chamber. The DP uses high quality pump oil (Santovac 5) and is water-cooled and backed-up by a Welch Duoseal Vacuum pump (Model 1373). This pump is used to rough out the source chamber and TOF region during experiments and maintenance by a manual flip switch that opens a bellows valve (KF50 flanges). During experiments, the pneumatic valve is open, and the DP is on, otherwise these are kept closed and turned off.

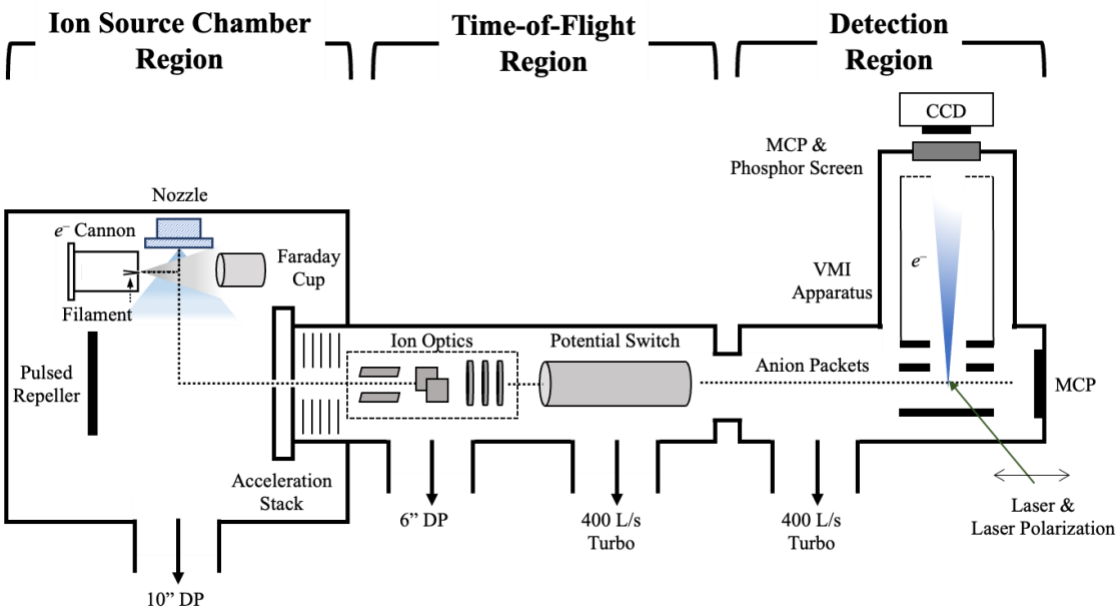

Figure 2.1: Photoelectron imaging spectroscopy schematic. There are three main sections: ion source chamber, time-of-flight, and detection region. Vapors are disputed from the nozzle and interacts with electrons from the electron cannon. Anions are repelled into the TOF-MS. A laser intersects the targeted anion to photoeject an electron. The electron is imaged by a CCD camera.

The time-of-flight mass spectrometer (TOF-MS) region is connected to a turbomolecular pump (TMP; Oerlikon Leybold Turbotronik 361; pumping speed: ~400 L/s) and a 6-inch DP that brings this region to a base pressure of $1–4\times10^{-7}$ Torr. The DP is water cooled as well. The TMP is backed by a single rotary pump (Leybold model Trivac B D16B; pumping speed: 13.4 cfm). A pneumatic gate valve (Chicago Allis Manufacturing, 6-inch model) is used to separate the DP from the TOF region. Like the source chamber region, the valve is only open when experiments are running, otherwise it is kept closed. The detection region is at a base pressure of $1–5\times10^{-9}$ Torr using another TMP (Leybod model Trivac B D16B) and backed by the same rotary pump as the TOF region.

2.2 Ion Source Chamber

A plasma chemical reaction is produced in the source chamber when the supersonic expansion of the sample vapors is intersected by an electron beam from an electron source, either an electron gun or electron cannon. A faraday cup (inside the source chamber) connected to a multimeter (outside the source chamber) is used to observe the current output by the electron source as well as collect the remaining electrons. The faraday cup is positioned in front of the electron source. As the expansion plasma travels down from the impaction region, the expansion reaches the reflector plate described in Section 2.3.

2.2.1 Electron Gun vs. Electron Cannon

There are two electron source designs used in this work: the electron gun and the electron cannon. A common similar design used in the photoelectron imaging spectroscopy community is the electron gun, which is shown on the left side of Figure 2.2. Detailed explanations and technical

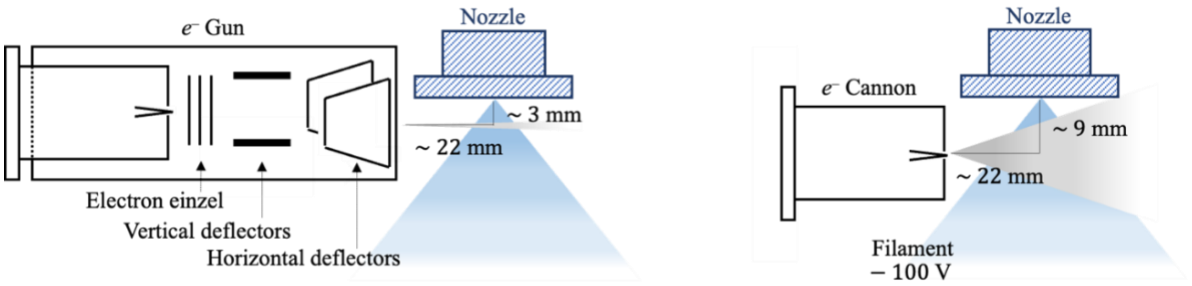

Figure 2.2: Electron gun vs. electron cannon. The electron gun (left) has more optics to align and focus the electron beam compared to the electron cannon (right). The optics are the electron einzel, vertical deflectors, and horizontal deflectors.

parameters of these two set-ups are explained elsewhere and in Section 2.6.[10, 12] The gun allows tunability of the electron beam, creating a focused and directed beam. However, difficulties of finding the signal are higher due to trying to optimize the electron beam. The electron cannon is used for the experiments discussed in this dissertation. The electron cannon set-up shown on the right in Figure 2.2 allowed the creation of hot phenide ions as discussed in Chapter 4. The electron cannon is like the electron gun except with the optics removed. The cannon provides a spray of electrons being able to bombard more of the supersonic gas expansion, creating more ions due to the increase of area. The distance of the electron cannon from the nozzle may vary slightly from each experiment.

2.3 Time-of-Flight Mass Spectrometer

The TOF-MS consists of a reflector plate, accelerator stack, two sets of deflectors, einzel lens, the potential switch, and a dual microchannel plate (MCP) detector. The reflector plate extract anions from the plasma into a Wiley-McLaren type TOF-MS.[13-14] Anions are accelerated by the accelerator stack and focused horizontally and vertically by the deflectors. Ions are focused by the einzel lens, gated with the potential switch, and detected by the MCP detector.

The reflector plate is used to optimize the ion focusing. The reflector plate is controlled by a pulse generator module (Direct Energy Inc., model PVM-4210) to bring a constant on/off time cycle of <20 ns. The voltage for the reflector plate ranges from –200 to –800 V. The reflector plate is powered by the float power supply for the ion optics. Anions are accelerated in the accelerator stack connected by a 1 MΩ laser-spiraled high precision resistors. The first plate is grounded, and the tenth plate (the last plate) is connected to a high-voltage DC power supply (37 Hewlett Packard 6516A) at +1950 V. After the accelerator stack, two sets of parallel deflectors direct the ions

vertically and horizontally by applying a ±0-135 V against the float voltage. The deflectors are operated by Agilent E3612A power supplies and floated by the HP power supply.

The einzel lens are used to direct the ion beam pathway and focus spatially. The three einzel lens has a 1.5-inch OD SS cylinder, 1.5-inch OD long, and separated by 0.160-inch Teflon. The voltages of the outer electrodes and middle electrode are +1950 V and +500-1000 V, respectively, powered by a Bertan model 250B-03R power supply. Anions enter the potential switch and are separated by mass to charge ratio in time. The potential switch is controlled by a high-voltage pulse generator (Direct Energy, Inc., model PVM-4140) and is synchronized with the reflector plate as it fires, floating to +1950 V with a rise time of ~15 ns. After 4-20 μs delay, the potential switch drops to ground immediately with anions still in the tube. The falling edge keeps unwanted mass from coming into the potential switch.

The targeted ions arrive in the detection region and hits the Chevron-type dual MCP detector.[10-11] The detector is floated by a split potential (Bertan, model 05B-03R) between 1 kV to the front and 2.5 kV to the rear of the MCP plates, which accelerates the electron cascade through the channels. An electric signal is generated when the electron cascade hits an anode that is floated ~200 V above the second MCP. This output is increased by a factor of 100 using an amplifier (Philips Scientific, model 6931). An oscilloscope (Tektronix, Inc., model 3032) is used to detect the ion signal intensity as a function of time.

The time-of-flight is converted to a mass scale using the Equation 2.1. below:

$$t = a\left(\frac{m}{z}\right)^{1/2} + t_0 \qquad (2.1)$$

where t is the time-of-flight and m/z is the mass-to-charge ratio for the targeted anion. The constant a and t_0 can be solved when m/z for two peaks (m_1/z and m_2/z) are assigned to their respective

measure times-of-flight (t_1 and t_2). These can be seen in Equation 2.2 and Equation 2.3. For a good calibration of the mass spectrometer, t_0 should be as close to zero as possible and around 2–3 $(\mu s)^{-2}$.

$$a = \frac{t_2 - t_1}{\sqrt{m_2 - m_1}} \tag{2.2}$$

$$t_0 = t_1 - a \tag{2.3}$$

2.4 Lasers

The laser beam lies in the same horizontal plane and perpendicularly intersects the ion expansion in the detection region. A beam with a diameter of ~5 mm enters the instrument through a silica window at a Brewster's angle of 55.5º to minimize reflections of glass. A copper tube is used as a beam dump located at the exit of the instrument. Two types of lasers are used for these experiments: Nd:YAG and dye lasers. Both types of lasers are triggered using a Stanford delay generator's internal timing. More details of the laser timings and specifications are described elsewhere.[10, 12]

2.4.1 Nd:YAG Laser

Most experiments done in this lab are photoejected with an neodymium-doped yttrium aluminum garnet (Nd:YAG) laser (Spectra-Physics, model Quanta-Ray Lab 130-50). This laser outputs 1064 nm with an energy of 200 mJ/pulse. A second harmonic can be produced by using a type II dideuterium (KDP) crystal to achieve a 532 nm with an energy of 70 mJ/pulse. A 355 nm with 30 mJ/pulse is generated by a third harmonic and a 266 nm with 15 mJ/pulse by a fourth harmonic. The laser output ~10 ns pulses with a 50 Hz repetition rate.

2.4.2 Dye Laser

The second laser that is used in this lab is the ND6000 dye laser (pumped by Surelite II-20 Nd:YAG; Continuum, Inc.), is used for adjusted wavelengths. The dye laser is capable of a broad spectrum based off the dye being used. A single wavelength can be selected using the angle of a motorized diffraction grating. Rhodamine 640 outputs a range of 607 nm to 622 nm. The peak of Rhodamine 640 is used to produce the 611 nm for the experiments discussed in the following next chapters. The laser output ~1 ns pulses with a 20 Hz repetition rate.

2.5 Photoelectron Spectroscopy *via* Velocity-Map Imaging

The detection region of the instrument starts with the velocity map imaging (VMI). This consists of three oxygen-free high conductivity copper plates of 1/32" thickness with a 1" diameter opening. The plates are stacked through #0-80 molybdenum threaded rods and nuts with alumina spacers and washers (Kimball Physics, Inc.) to isolate each plate from the rods. The high work function ~4.7 eV of these materials decreases the chances of introducing foreign ions from material surfaces into the experiment. The ion beam is intersected by the laser between the second and third plates of the VMI starting from the top. The top plate has a positive potential of 300–1000 Volts as it encounters the free electrons. The second plate is grounded due to contact with the metal rods. The third plate has a negative potential of 100–350 Volts to send the photodetached free electrons into a ~15.5 cm TOF tube. The typical ratio used is the top plate at –330 V and third plate at +900 V.

The imaging region starts with the dual chevron-type MCP detector with a phosphor screen (P47) anode coupled to a fiber optic vacuum window (Burle, Inc.). The phosphor screen is held at +6.5 kV and MCP at +3 kV. A CoolSnap HQ CCD camera (Roper Scientific) is used to acquire

photoelectron images. The collection time for these images varied between 1-5 minutes. A background image was collected for each image by offsetting the laser and MCP pulse timing by $\pm$100 ns. The background images were subtracted from the signal images in the Cool Image program.[15] Background-subtracted images were summed up to achieve a better signal-to-noise image, ranging from 50-100 minutes of total collection time.[12]

Furthermore, experimentally, the photoejected electron expands as a three-dimensional wave front and is collapsed as a delta function when contacted with the detector. Over several thousand iterations, a raw photoelectron image is formed. BAsis Set EXpansion (BASEX) program from Reisler and co-workers is used to analyze these photoelectron images.[16] This program takes the two-dimensional projection of a three-dimensional image collapsed into an image using Abel-transformation.[17] The photoelectron angular distribution is analyzed in a self-written MATLAB script that can be found in Appendix A1, which is previously based on the BetaCalc program.[15]

2.6 Ion Formation

A pulsed nozzle valve (General Valve, Series 9) with an orifice of ~800 μm is used to create a conical half-angle of 45º supersonic expansion of the sample gas. The gas flow through the valve orifice is controlled by the magnetic force of a solenoid to lift a spring-loaded poppet (Kel-F or PEEK). The IOTA ONE high speed valve driver (Parker Hannifin Corp., General Valve) is used to fire the nozzle and to set a 1-3 ms delay timing between the trigger pulse and nozzle opening to increase the stability of ion formation signal. The nozzle is externally triggered by a TTL pulse (T_0) from a delay generator (Stanford Research Systems, Inc., model DG535). The nozzle valve is triggered at 50 Hz with the opening time of 150–250 μs. The duty cycle of the ion

formation is ~1%. The total experimental period is 200 ms. When the nozzle is operating, the source chamber pressure increases to $1–5\times10^{-5}$ Torr from $\sim5\times10^{-7}$ Torr and the detection region pressure increases to 3×10^{-8} Torr from $1–5\times10^{-9}$ Torr. The nozzle is grounded to avoid charges of the electron beam from the electron gun or electron cannon.

Both the electron gun and cannon are positioned perpendicular to the nozzle orifice. The electron gun is described first as the electron cannon was derived from the electron gun. The electron gun is contained in a grounded shell. High energy electrons are produced when a current of 3–3.5 A passes through a 1 mm wide bent thoria-coated iridium filament (e-Filaments, LLC). A small aperture is in the center of the grid where electrons can escape in a beam. The beam is accelerated by a ground cylindrical anode cup around the filament base followed by focusing options– Einzel lens that consists of three electrodes. The outer electrodes on the Einzel lens are referenced to ground while the middle electrode is adjustable between –500 and –1200 V (Keithley 247). This beam is guided by vertical and horizontal electrostatic deflector plates using ±0–135 V (Agilent, model E3612A). The electron beam intersects the supersonic expansion about 3–5 mm away from the nozzle orifice as shown in Figure 2.1.

The electron cannon is stripped-down ion optics version of the electron gun. This base of the electron cannon is the same as the electron gun with the same thoria-coated iridium filament but heated to 4–5 A direct current using a Kepco 15-15M current supply. The electron cannon and anode cup power supplies are floated between –100 to –1000 V (Bertan, model 205B-03R). The anode cup applies an additional potential that ranges from 0 to –200 V for this set-up. However, most experiments did not need or rely on the additional potential from the anode cup. The electron beam is positioned ~9 mm further down from the expansion as shown in Figure 2.1.

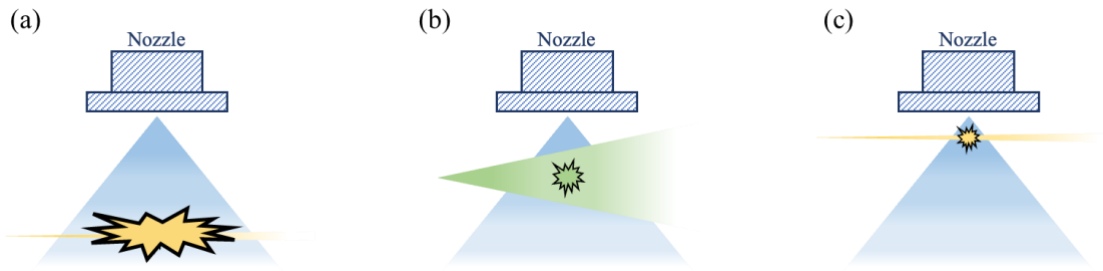

Figure 2.3: Impaction of electron beam and the supersonic expansion at different orientation. (a) An electron gun hits a dispersed area, creating few ions, resulting in low signal. (b) An electron cannon hits a dense area, creating many ions. (c) An electron gun hits a highly dense area, creating many ions. The temperature varies based off the distance between the intersection and nozzle.

This supersonic expansion produces a series of chemical reactions shown below: (2.6.1) deprotonation, (2.6.2) dissociative electron attachment, (2.6.3) slow secondary electron attachment, and (2.6.4) evaporative cooling.

$$XH + e^- \rightarrow (XH)^- \rightarrow X^- + H^+ \quad (2.6.1)$$

$$XY + e^- \rightarrow (XY)^- \rightarrow X^- + Y \quad (2.6.2)$$

$$X + e^- \rightarrow X^- \quad (2.6.3)$$

$$(X)_n + e^- \rightarrow [(X)_{n-m}]^- + mX \quad (2.6.4)$$

(X = target molecule, Y = functional group or other molecule, n = # of solvents)

The beam is caught by the Faraday cup detector at the end of the beam. An amp meter (Fluke Corp. multimeter, model 83 III) measures the electron flux between the cup and the chamber walls. All wire connections in the source chamber are Teflon coated and cables with crimped connection are used for lower outgassing properties.

2.6.1 Ion Temperature Control

The temperature of the ions could likely be controlled based off the distance of the electron beam from the nozzle expansion as shown in Figure 2.3 with the electron gun and electron cannon. It is possible that too much distance away from the nozzle orifice will likely decrease the number of ions produced- resulting in low signal output. Furthermore, the temperature of the ions can be controlled by increasing or decreasing the distance of interaction and the nozzle orifice. Initially, nascent ions are equally hot and what cools these ions are through subsequent collisions. This means that ions that are closer to the nozzle will have a longer cooling time through collisions and ions farther away will have a shorter cooling duration. This is a parameter to be continued and investigated for the near future.

Chapter 3: Dipole Effects on the Photoelectron Angular Distributions of SO^-

The concept of photoelectron angular distribution (PAD) was first mentioned in Chapter 1, where the Cooper-Zare central-potential model is typically used for a one-photon PADs in Equation 1.3, and this equation can be altered for a mixed-character orbital represented in Equation 1.5. The approximation for these equations is under the approximation that the departing electron has little to no interactions with the neutral residue. However, this approximation can become invalid if the exit-channel interactions cannot be disregarded, such as in the case of the neutral residue having a significant dipole moment.

In this chapter, the PADs were studied for SO^-, both experimentally and theoretically.[18] All calculations and modeling used Q-Chem 5.1 and *ezDyson* 5.0.[19-20] The equations mentioned earlier is not so straightforward for SO^- compared to other mixed character diatomic molecules. This is mainly due to the different principal quantum numbers of S (n = 3) and O (n = 2). Therefore, other approaches have been used to understand the PADs of SO^-. The interactions between the electron and dipole moment during photodetachment plays a significant role in shaping the PADs of SO^-. The studies of SO^- have helped further advance the understanding of dipole effects for PADs, especially for π^*orbital detachment. The σ orbital detachment was studied previously through the anion CN^-.[21] Moreover, SO^- vs. O_2^- PADs were compared due to O_2^- possessing no dipole moment to determine which two factors contributed more to the PADs differences: the shape of the photodetachment orbitals or the exit-channel interactions. It was found that for this comparison, the latter contributed mainly to the PADs differences.

Section 3.1 gives an overview of the importance of SO^-. Section 3.2 and Section 3.3 provides the experimental methods used and the experimental analysis, respectively. The experimental and theoretical discussions are mainly in Section 3.4 and Section 3.5. Here, the

different methods are used to analyze the experimental data with computational approaches. It is important to note that this Chapter is an overview that focuses on the main idea of how exit-channel interactions cannot always be ignored or assumed negligible.

3.1 Importance of SO^-

Sulfur monoxide has been studied mostly in the atmospheric and astronomy community. In the global sulfur cycle, SO is produced through ultralight photolysis of SO_2.[22-24] The consequences of this allows the oxidation of SO_2 and SO_3, both components in acid rain.[23, 25] It has been seen to be part of several photochemical processes in different terrestrial atmospheres. The photoionization of SO produces SO^+ occurs in interstellar space and Io's exosphere.[26-27] Furthermore, SO can undergo self-reaction to produce SO_2 and monoatomic oxygen.

$$SO + h\nu \rightarrow S + O \quad (3.1)$$

$$SO + SO \rightarrow SO_2 + O \quad (3.2)$$

The electronic states of sulfur monoxide and sulfur monoxide cation have been studied both experimentally and theoretically.[28-30] In photoelectron spectroscopy, Lineberger and coworkers studied SO^- photodetachment transitions of SO^- ($X\,^2\Pi$) $\rightarrow$ SO ($X\,^3\Sigma^-$, $a\,^1\Delta$, $b\,^1\Sigma^+$) obtained from their high-resolution energy spectrum and determined the SO adiabatic electron affinity at 1.125 eV.[31]

3.2 Experimental Methods

The experiment was carried out with the instrumentation described in Chapter 2, using the electron cannon configuration. Elemental sulfur dissolved in CS_2 at room temperature was used with carrier gases of either O_2 or CO_2 at ~1.4 atm. CO_2 carrier gas was used to obtain data at 532

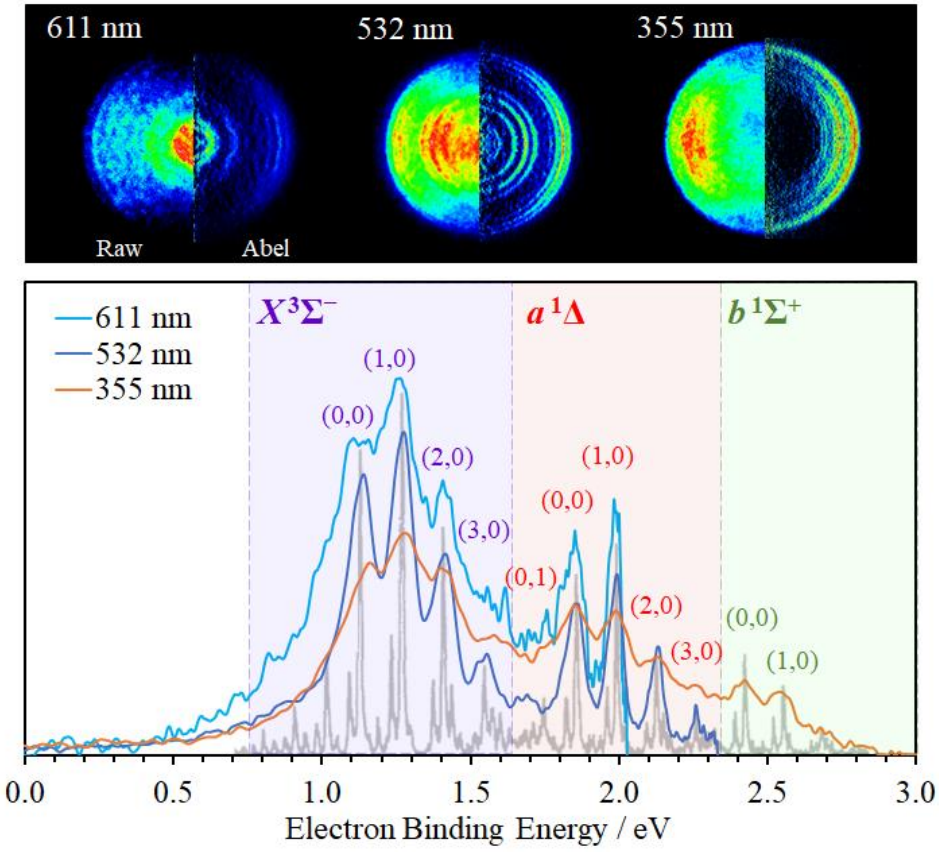

Figure 3.1: Photoelectron images and energy spectra of SO^-. (Top) The raw (left half) and inverse Abel transformation (right half) images of SO^- are captured at 611, 532, and 355 nm. (Bottom) The energy spectra correspond to the above images with SO ($X^3\Sigma^-$, $a^1\Delta$, $b^1\Sigma^+$; v') ← SO^- ($X^2\Pi_{3/2}$; v'') photodetachment transitions and with labeled format of (v',v'').

nm, and O_2 was used to obtain data at 611 and 355 nm. It was later found out that O_2 as the carrier gas produced more SO^- ions. The experiments at 532 and 355 nm used the Spectra Physics Lab-130-50 Nd:YAG at a repetition rate of 50 Hz using second and third harmonics, respectively. ND6000 dye laser with Rhodamine 640 dye pumped by Surelite II-20 Nd:YAG at a repetition rate of 20 Hz was used for 611 nm. The specifications for these lasers are described in Chapter 2. The laser polarization direction is parallel to the plane of all reported images. The raw photoelectron images (in Figure 3.1) undergo an inverse Abel transformation using the BASEX program from Reisler and co-workers[16-17] to further obtain the photoelectron spectra.

3.3 Experimental Results

Photoelectron images were collected at 611 (2.03 eV), 532 (2.33 eV), 355 (3.49 eV) nm for SO^-. In Figure 3.1 (top), raw photoelectron images are shown on the left half and the inverse Abel transformation images are shown on the right half. Chapter 2 discusses the details on the inverse Abel transformations. The corresponding energy spectra (Figure 3.1 bottom) are shown for each of these images, plotted with respect to electron binding energy (eBE), eBE = $h\nu$ − eKE. Hot bands are responsible for the left shoulders of the spectra. Here, we can see that three states are accessed: SO ($X^3\Sigma^-$, $a^1\Delta$, $b^1\Sigma^+$; v') ← SO^- ($X^2\Pi_{3/2}$; v'').

The spectra of SO^- were compared to a higher resolution spectrum at 351.1 nm (3.531 eV) by Lineberger and co-workers represented in the same figure in grey.[32] The energy spectrum has highlighted regions showing which electronic states were accessible for which wavelengths of light. The $X^3\Sigma^-$ and $a^1\Delta$ electronic states of SO were accessed for 611, 532, and 355 nm. The $b^1\Sigma^+$ electronic state of SO was accessed only at 355 nm. The experimental data peaks were assigned based off the spectrum of Lineberger and co-workers mentioned earlier.

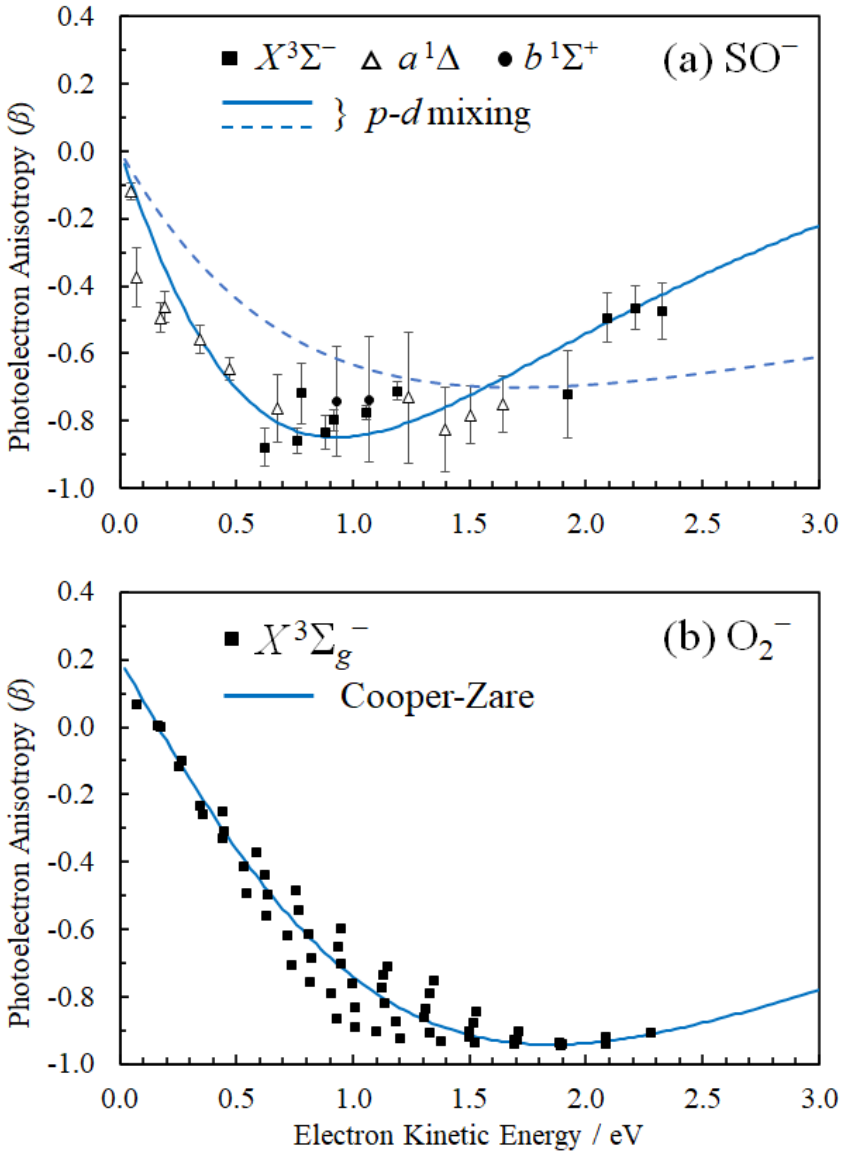

Figure 3.2: Photoelectron angular distributions of SO^- and O_2^-. (a) Beta values are from the experimental data in Figure 3.1 for 611, 532, and 355 nm. The blue solid line represents the 2*p*-3*d* mixing curve using Equation 1.5. The dashed curve is explained in detail in the paper. (b) The curve for O_2^- is described by Hanstorp's implementation of the Cooper-Zare equation (Equation 1.5) with $A_2 = 0.36\ \text{eV}^{-1}$ and $\cos\delta_{3,1} = 0.96$.

The PADs were obtained from the photoelectron images of each peak using Equation 1.6 and can be seen in Figure 3.2 as data points. PADs were calculated from raw experimental images using the MATLAB code that can be found in the appendix of this dissertation. The background information about PADs can be found in Section 1.4. More discussion about experimental PADs and computational modeling PADs follows in the next couple of sections.

3.4 Discussion: Experimental and Computational PADs of SO^- vs. O_2^-

As mentioned before, PADs are used to understand the properties of molecular orbitals from which the electrons are ejected. The common approximation used to understand PADs expressed in Equation 1.6, which cannot be used to correctly model SO^-, unlike O_2^-, due to a significant dipole moment as described and having multiple *l* (orbital angular momentum quantum number) values to describe the function. This is similar to other molecules like NO^- and HO_2^-.[33] Therefore, in Figure 3.2, the solid blue line is used only for comparing the trends between SO^- vs. O_2^-. The solid blue line represents a *2p-3d* mixing with $\gamma_d = 0.81$, $A_1 = 0.53\ \text{eV}^{-1}$, $A_2 = 0.36\ \text{eV}^{-1}$, $B_2 = 11.4\ \text{eV}^{-1}$, and $\cos\delta_{2,0} = \cos\delta_{3,1} = 0.96$. The blue dashed curve is used to guide the analyses by the other collaborators on this project.[18] The PADs of O_2^- for $X^3\Sigma_g^- \leftarrow X^2\Pi_g$ was reported by Van Duzor *et al*.[34] The solid blue lines for both SO^- and O_2^- have the same general trend, with SO^- shifted to the left.

3.5 Discussion: Theoretical Modeling of SO^- PADs

3.5.1 Modeling PADs of SO^- without Electron-Dipole Interactions

The *ab initio* calculations of the PADs of SO^- reported here neglect the interactions of outgoing electron with the dipole moment of the neutral residue. Geometry optimization of SO^-

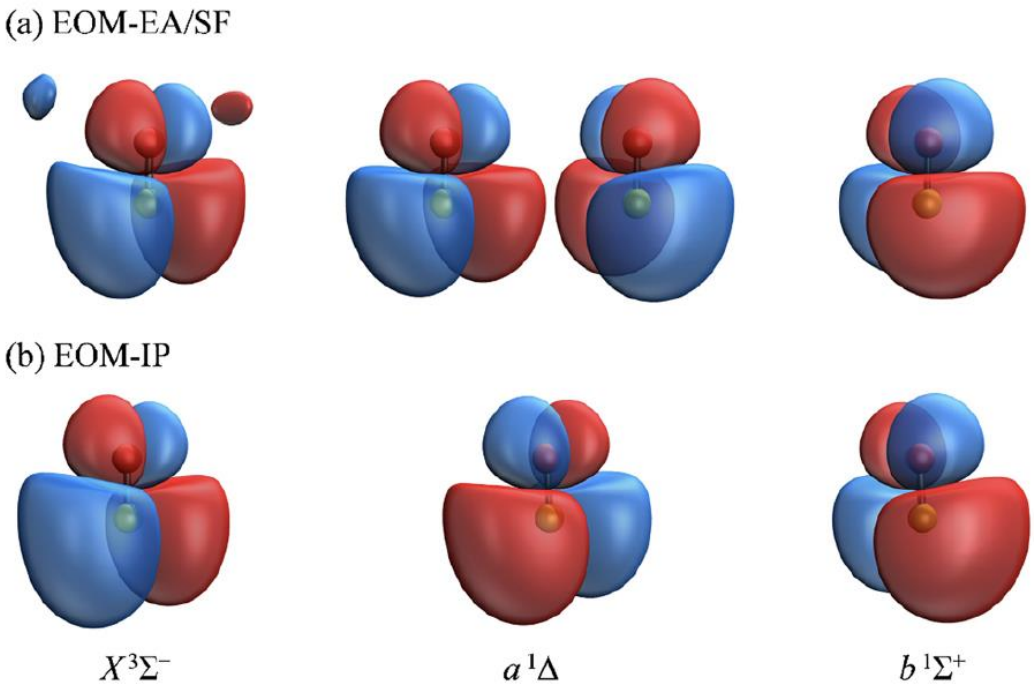

Figure 3.3: Dyson orbitals of the detachment transitions from SO^- to SO. The detachment transition between SO^- ($X^2\Pi_{3/2}$) to neutral SO ($X^3\Sigma^-$, $a^1\Delta$, $b^1\Sigma^+$). Geometry optimization on SO^- were performed at CCSD(T) method and aug-cc-pVTZ+5s5p5d5f basis sets. Section 3.5 explains the details of "5s5p5d5f". Orbitals obtained in (a) were calculated using EOM-EA/SF, which refers to the transition from EOM-EA-CCSD to EOM-SF-CCSD states. This starts with the neutral SO as a reference. Orbital calculated in (b) used EOM-IP-CCSD and uses the anion as the starting reference. Isosurface values = 0.02.

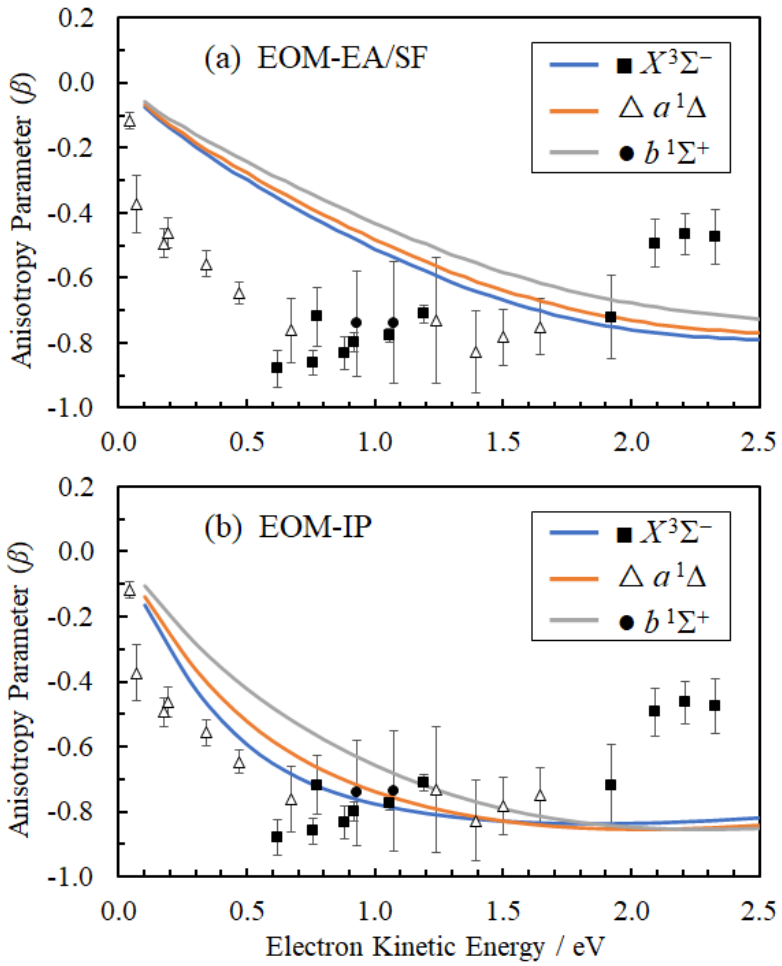

Figure 3.4: Photoelectron angular distributions of SO^- using EOM-EA/SF and EOM-IP. The black solid curve uses the Cooper-Zare-Wigner-Bethe equation as a reference for the trend. Dyson orbitals and HF calculations were carried out in *ezDyson*. Dyson orbitals are labeled as *ezDyson* and HF calculations as HF in the legend. Colored solid lines use Dyson orbitals without diffuse basis sets. Colored dotted lines use Dyson orbitals with diffuse basis sets. Colored dashed lines use Hartree-Fock calculations. 5spdf means that 5 diffuse basis sets were added to each *l* value shown (*s*, *p*, *d*, *f*).

was first performed with method and basis sets of CCSD(T)/aug-cc-pVTZ using Q-Chem 5.1. For the optimized geometry, the Dyson orbitals[35-38] of each SO ($X^3\Sigma^-$, $a^1\Delta$, $b^1\Sigma^+$) ← SO^- ($X^2\Pi_{3/2}$) transitions were calculated *via* equation-of-motion (EOM-CCSD) methods. As mentioned earlier, Dyson orbitals, ϕ^d, is defined as overlap of the many-body wavefunctions of the initial N-electron and final $N-1$ electron state:

$$\phi^d = \sqrt{N} \int \left(\Psi_f^{N-1}(2, \dots, N)\right)^* \Psi_i^N(1, \dots, N)\, \mathrm{d}2 \dots \mathrm{d}N \qquad (3.3)$$

Two different EOM calculations were performed with the first being electron attachment (EOM-EA-CCSD) and spin-flip (EOM-SF-CCSD) for SO^- ($X^2\Pi_{3/2}$) and SO ($X^3\Sigma^-$, $a^1\Delta$, $b^1\Sigma^+$), respectively.[39-40] The second approach being ionization-potential (EOM-IP-CCSD), which uses the anion as the reference to access the three neutral states of SO. Furthermore, CCSD/aug-cc-pVTZ+5s5p5d5f basis set was implemented in most of the calculations to introduce diffuse orbitals. This basis set modified the general aug-cc-pVTZ with the additional five s, five p, five d, and five f diffuse functions by scaling each successive factor exponent by one half. The Dyson orbitals using EOM-EA/SF and EOM-IP can be seen in Figure 3.3 with further details in the paper.[18]

The Dyson orbitals obtained from Q-Chem are used as inputs for the program *ezDyson* 5.0 to calculate the photoelectron anisotropy shown in Figure 3.4.[20] It is apparent right away that the *ab initio* calculations disagree with the experimental PADs by shifting the location of the minimum of the anisotropy parameter trend vs. eKE. Other methods and basis sets were attempted (not shown here), but also did not produce similar trends as the experimental data. Due to the significant discrepancy between experimental and *ab initio* calculations *via ezDyson*, other computational methods and models were needed to describe the photodetachment process.

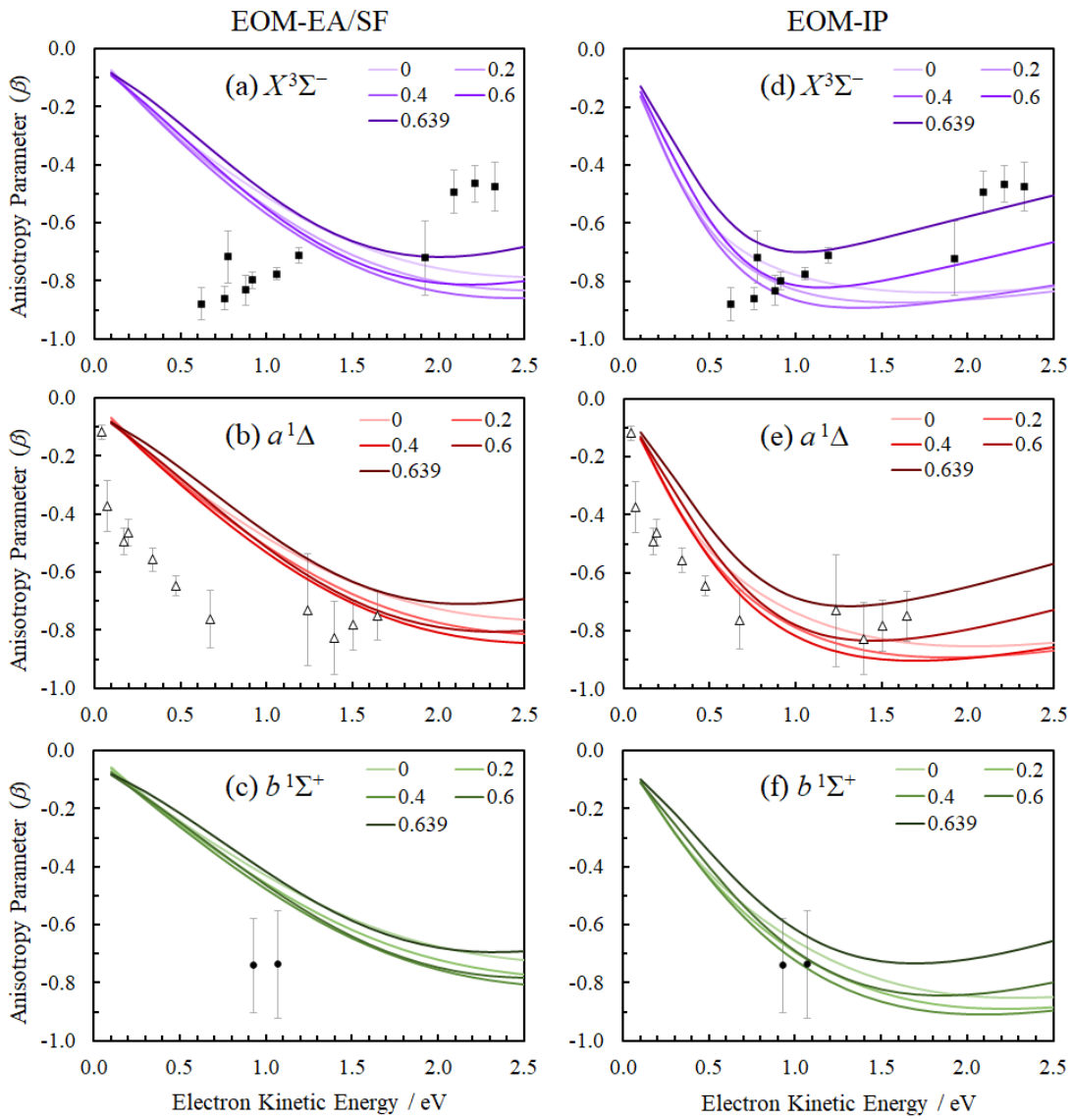

Figure 3.5: Experimental and computed point dipole-field model PADs of SO^-. (a) and (d) are $X^3\Sigma^-$, (b) and I are $a^1\Delta$, (c) and (f) are $b^1\Sigma^+$. The left column was calculated using EOM-EA/SF-CCSD Dyson orbitals, and the right column was calculated using EOM-IP-CCSD. These calculations used the aug-cc-pVTZ+5s5p5d5f basis sets. These PADs calculations varied point dipole strength (a.u.) at 0, 0.2, 0.4, 0.6, and 0.639.

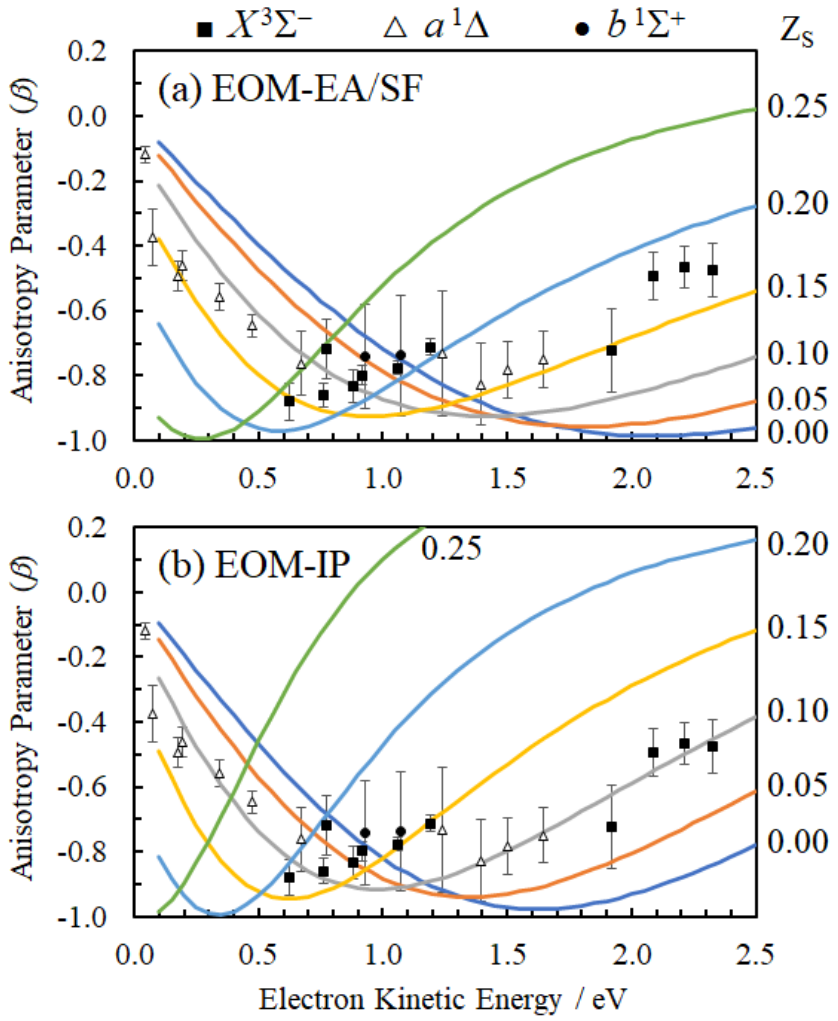

Figure 3.6: Experimental and computed multi-center Coulomb wave model PADs of SO^-. (a) Calculations used were EOM-EA-CCSD to EOM-SF-CCSD Dyson orbitals. (b) Calculations used were EOM-IP-CCSD. All calculations used the general standard aug-cc-pVTZ. Charges for Z_S and Z_O were varied for the photodetachment to the $X^3\Sigma^-$ state of SO and the varied charges of Z_S are shown on the right side of the graph.

3.5.1 Modeling PADs of SO^- including Electron-Dipole Interactions

In the previous section, *ab initio* calculations neglecting electron-dipole interactions were performed on SO^-; however, the results were significantly different when compared to the experimental PADs. This suggests that dipole effects may play an important role and need to be accounted for in the calculation. With the help of collaborators[18], we were able to model the effects of electron-dipole interactions in SO^- photodetachment.

There were two approaches that fit the experimental results well: the first approach assumed that the outgoing electron is a superposition of eigenfunctions of a point dipole-field Hamiltonian, and the second approach represented the departing electron in terms of Coulomb waves emitted from two distinct charged centers: a partial positive charge on the sulfur atom and an equal partial negative charge on the oxygen atom. In Figure 3.5 and Figure 3.6, the computational methods of point dipole-field and multi-center are compared with the experimental data, respectively. These calculations were carried out by our collaborators at University of Southern California, Washington University, and Georgia State University[18] and therefore not described here in detail. Only a brief explanation of the results follows.

The point dipole moment approach shows the importance of electron-dipole interactions in photodetachment as shown in CN^- and now SO^-. The dipole moment of CN was 1.45 Debye for the $X\,^2\Sigma^+$ state.[41] SO has a similar dipole moment, 1.55 Debye for the $X\,^3\Sigma^-$ state.[42] These calculations also used the aug-cc-pVTZ+5s5p5d5f basis sets that was explained earlier. This approach was implemented for several dipole-moment values to the neutral reside. The illustration of the importance of electron-dipole interactions in photodetachment is shown in the paper in Figure 9 (not shown here) by comparing when $D = 0$ and $D = 0.60$ a.u. (D = magnitude of the dipole moment).[18] The variations of D is seen in Figure 3.5, where the curve deviates from the

free-particle limit as D increases away from zero. Furthermore, increasing D causes the β minimum to shift to the left or to lower eKE and narrowing the curve. The depth or minimum of β is increased only up to when D is ~0.4 a.u. and the trend is reversed as D continues to increase. In the point-dipole field, when D approaches the critical value of $D_c = 0.6393$ a.u. for binding an l = 0 electron, the parametric trend curve accelerates.[43] Once pass the critical value, the point-dipole model breaks down and is explained further in the paper and elsewhere.[18, 44] The critical value, D_c, for binding an electron is based on the fixed-dipole approximation.[43]

The dipole moment for the neutral equilibrium geometry of SO at $X\,^3\Sigma^-$ state is 0.610 a.u. and $a\,^1\Delta$ state is 0.52 a.u.[42] However, photodetachment is a vertical process where the neutral states are at the anion geometry. The dipole moment, calculated at CCSD/aug-cc-pVTZ, for SO at $X\,^3\Sigma^-$ state and $a\,^1\Delta$ state increases by 0.16 a.u. and 0.22 a.u., respectively. This increase is due to the elongated bond length of the anion causing a larger charge separation. Overall, the point-dipole model showed how important it is to consider the interactions between the neutral residue dipole moment and the leaving electron.

The next method is the multi-center approach uses partial charges of Coulomb-wave expansion of the photoejected electron on the center of each atom.[45] This is done by splitting the molecular Dyson orbitals into parts corresponding to the center of each atom *c*:

$$\phi^d = \sum_c \phi_c^d \tag{3.4}$$

Equation 3.4 provides a sum of individual atoms to determine the total photoelectron dipole matrix. The calculations used the general standardized aug-cc-pVTZ to avoid diffuse function artifacts from electron density that is far from the center of the atoms. Oxygen is more electronegative than sulfur; therefore, the negative charge lies on oxygen and positive charge on sulfur. For EOM-

EA/SF, the best agreement to the experimental data was when $Z_S = 0.15$ and $Z_O = -0.15$ and for EOM-IP, it was $Z_S = 0.10$ and $Z_O = -0.10$, as shown in Figure 3.6. As mentioned earlier, the neutral equilibrium geometry of SO dipole moment at $X\,^3\Sigma^-$ state is 0.610 a.u and $a\,^1\Delta$ state is 0.52 a.u.[42] Dividing by the obtained CCSD/aug-cc-pVTZ calculated equilibrium bond length of SO^-, 1.592 Å, we get the partial charge on sulfur approximately $Z_S = 0.20$ and $Z_S = 0.17$, respectively. The partial charge values are closer to the values obtained in EOM-EA/SF-CCSD system; however, this does not disregard the EOM-IP-CCSD system as less accurate, but rather coincidental.

When comparing the two models, point dipole and multi-center, they are quantitatively different due to the diffuseness of the Dyson orbital; however, both models follow the same trend with increasing the value on Z_S, the minimum of the anisotropy parameter is shifted to the left (i.e., lower eKE). Extensive details about these calculations were performed by Krylov and co-workers, Mabbs and co-workers, and Gozem and are described in detail in the paper.

3.5 Conclusion

Sulfur monoxide anion was studied *via* photoelectron imaging spectroscopy and *ab initio* modeling. Specifically, the PADs of SO^- was compared experimentally and computationally as well as comparing to previous studies of O_2^-.[46-48] The photodetachment accessed the electronic states of SO: $X^3\Sigma^-$, $a^1\Delta$, and $b^1\Sigma^+$. Moreover, SO^- detachment is from a π^* orbital and has similar conclusions as the previous studied CN^-, which is a σ detachment. Here, SO^- extends the dipole-field model studies by providing a non-σ detachment.

When the PADs of SO^- vs. O_2^- were compared, in Figure 3.2, it was seen that both have similar trends using the Cooper-Zare curve with SO^- shifted to the left or a smaller eKE. As

mentioned repeatedly, the Cooper-Zare curve on SO^- is used figuratively. The main difference between the two anions is the presence of a dipole moment. The results of this comparison showed that exit-channel interactions play an important and significant role in understanding the PADs of SO^-.

Furthermore, the computational models that disregards electron-dipole interactions will result in incorrect data when compared to SO^- experimental data as seen Figure 3.4. The modeled photoelectron anisotropy minimum is underestimated and plateaus at a higher eKE above 1.5 eV. Including SO dipole moment into the PAD calculations yielded in fair agreement when compared to the experimental PADs data. The models used were the point dipole-field model with $D > 0.6$ a.u. and the multi-center model with $Z_S = 0.10 – 0.15$. Both models are consistent with the experimental PADs data. Furthermore, generalized models show there are limitations, in this case, SO^- could not be used with the generalized Cooper-Zare model such that other approaches mentioned earlier were used instead.

Chapter 4: Photoelectron Spectroscopy of Hot Phenide: Experiment and Statistical Analysis

In Chapter 3, we saw the limitations of a generalized PAD model, not accounting for exit-channel interactions, in the case of a system possessing a significant dipole-moment. Here, we peer into how temperature can make a common approach to calculating the Franck-Condon (FC) factors unfeasible.[49] A common method that is used to calculate the FC factors[50-52] calls for a state-specific approach, best applicable to cold anions with most population in the ground vibrational state. This creates a limitation when trying to understand hot ions. We propose a statistical approach instead of a state-specific approach to model the dense photoelectron spectra obtained for hot polyatomic ions.

A state-specific approach would result in millions of years to converge, while a statistical approach can give results in matter of minutes or hours depending on the parameters.[49] With these methods, spectral modeling estimated the temperature of phenide ($C_6H_5^-$) around 700 K. In this chapter, isolated ions of hot phenide are the focus, unlike Chapter 5, where hot phenide with water will be analyzed to understand microhydration interactions. Section 4.1 briefly discusses the general importance of phenide and hot polyatomic ions. Section 4.2 and 4.3 touch on the experimental methods and experimental results, respectively. Section 4.4 dives into the FC simulations as well as the statistical methods used for hot phenide. Section 4.5 describes how a combination of FC simulations with a statistical approach can help determine the temperature from a congested photoelectron energy spectrum. This chapter does not go into in-depth details about the processes of each statistical method (i.e., the detailed explanations are found within the published paper), but rather explains and supports the need for statistical methods in hot ions due to complications such as unreasonable computation time.

4.1 Importance of Phenide and Hot Ions

Phenide is deprotonated benzene $C_6H_5^-$ (abbrev. Ph^-). Its photodetachment produces a phenyl radical or Ph, which is an important intermediate in forming polycyclic aromatic hydrocarbons (PAHs).[53] In combustion reactions, gaseous PAHs are one of the precursors of soot particles.[54-56] In addition, PAHs are involved in many chemical and photochemical processes and interactions in interstellar mediums.[57-61] Not all of these chemical reactions occur at cold or room temperature environments, such that making hot species important to understand and study.

In the photoelectron spectroscopy community, it is uncommon and not the primary focus to study hot molecules or ions. Understanding the photoelectron energy spectra of cold species is simpler compared to the spectra of their hot counterparts. The density of states (DOS) of a polyatomic molecule or ion increases rapidly with excitation energy- effecting the thermodynamic and spectroscopic properties of thermally excited ensembles.[62-64] The spectra of hot ions may have broadening and appear congested due to the presence of hot bands. Several methods of spectral modeling were used to help understand and interpret these hot spectra, specifically for hot phenide.

The energy distribution at thermodynamic equilibrium is generally described by the Boltzmann equation:

$$P(E) = cg(E)e^{-E/kT} \tag{4.1}$$

where E is the excitation energy, c is the normalization constant, $g(E)$ is the DOS, k is the Boltzmann's constant, and T is the absolute temperature. The DOS, $g(E)$, in Equation 4.1 can increase rapidly with energy, shifting the $P(E)$ population maximum from E = 0 to multiples of kT at moderate temperatures. Therefore, many (millions) of initial states may have to be included in direct FC calculations, which can limit state-specific approaches. For example, the complete FC analysis of all significant vibrational states of phenide at T ≈ 1000 K would require millions of

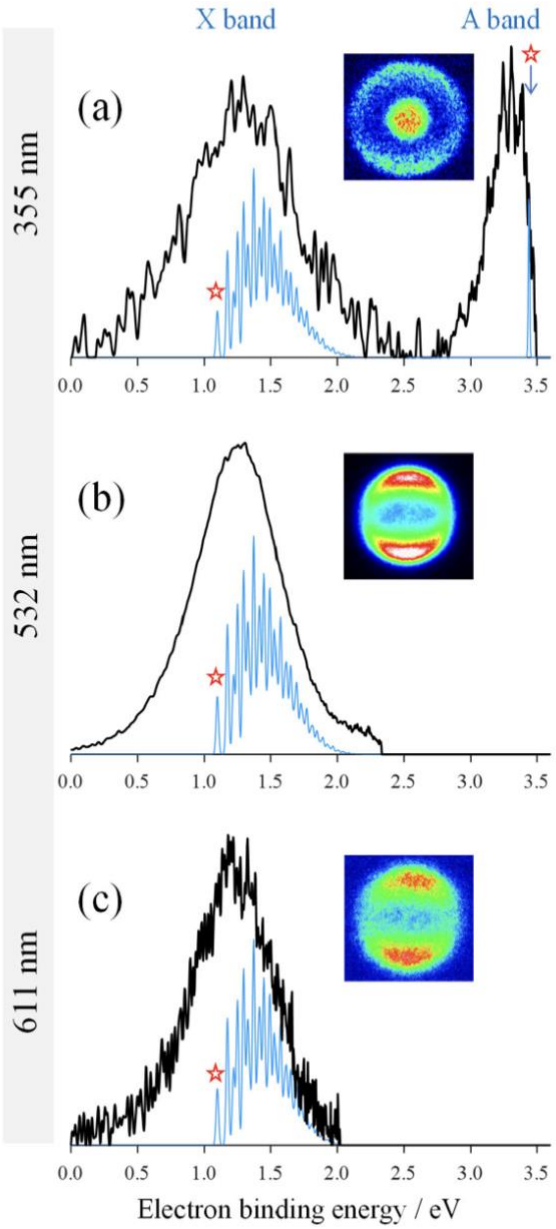

Figure 4.1: Photoelectron energy spectra and images of Ph^-. Spectra and images were obtained at (a) 355 nm, (b) 532 nm, and (c) 611 nm light. The black line is the experimental data, and the light blue line indicates the model spectra of cold phenide. The stars listed on the graphs mark the corresponding transition origins with the left side of the star being hot bands. The X and A band shown in 355 nm is the ground electronic state and the first excited state of the phenyl radical, respectively.

years to compute (as mentioned later in section 4.4.2). Thus, a realistic approach not completely relying on state-specific calculations is needed. Three active-modes models are used here to help analyze and understand the energy spectra of hot phenide. We term them as active modes + dark bath, active modes + bright bath, and the energy conservation model. They will all be discussed later in this chapter.

4.2 Experimental Methods

The specifications of the photoelectron imaging instrumentation used are explained in detail in Chapter 2. The precursor sample used was benzeneselenol or selenophenol (PhSeH) with argon as the carrier gas at 1.8 atm backing pressure. The electron cannon set-up was important in creating hot phenide ions in this study (described in Section 2.2.1). The electron cannon was positioned with its axis perpendicular to the nozzle and in-line with the faraday cup. The electron cannon was approximately 10 mm in front of the nozzle and 20 mm to the right of the nozzle. The specification for the nozzle is described more in Section 2.6. Anions were separated in time according to their mass in a Wiley-McLaren TOF mass spectrometer.[13] Phenide was intersected by a pulsed laser in the detection region to photoeject an electron. Spectra Physics Lab- 130-50 Nd:YAG laser (repetition rate: 50 Hz) produced 532 nm and 355 nm light pulses as a second and third harmonics, respectively. Rhodamine 640 dye in a ND6000 dye laser produced the 611 nm light by second harmonic of the Surlite II-20 Nd:YAG laser (repetition rate: 20 Hz). Further laser specifications are described in Section 2.4. Ejected photoelectrons were imaged using the VMI assembly discussed in Section 2.5. The photoelectron images for phenide at the mentioned wavelengths were acquired and shown in Figure 4.1. The photoelectron spectra were obtained *via* an inverse Abel transformation using the BASEX program from Reisler and co-workers.[16-17]

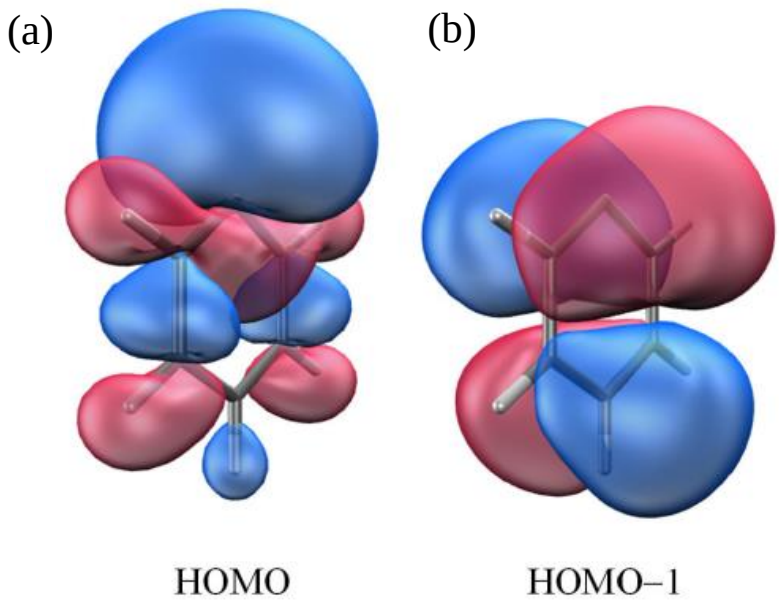

Figure 4.2: Canonical Hartree-Fock molecular orbitals of Ph^-. Phenide has a closed-shell electron configuration to the $X\,^1A_1$ electronic state. The optimized anion geometry was calculated with the aug-cc-pVDZ basis set. Isosurface value = 0.04. (a) The a_1 HOMO has a σ character and (b) the b_1 HOMO-1 has a π character.

4.3 Experimental Results

The photoelectron energy spectra and raw images of phenide ions collected at 611 nm (2.03 eV), 532 nm (2.33 eV), and 355 nm (3.49 eV) are shown in Figure 4.1. A simulated FC spectrum of cold phenide is plotted on the same graph in light blue as reference and hot phenide spectra in black with respect to the electron binding energy. The left shoulders of all these experimental spectra consist of hot bands, which indicates that these phenide ions are at high temperatures. The transition origins are indicated by a red star on the reference cold spectra. The photoelectron spectrum at 355 nm has two electronic bands, marked X and A. These bands correspond to the ground and first excited electronic state of phenyl, respectively. The spectra at 532 nm and 611 nm only show the X band, corresponding to the ground state of phenyl.

The laser polarization is vertical in plane with the images shown. The photoelectron image of phenide at 355 nm reveals a parallel PAD character for the X band and an isotropic character for the A band. Optimization and frequency calculations on phenide were carried out using Q-Chem 5.1 with method/basis set of B3LYP/aug-cc-pVDZ and EOM-IP-CCSD/aug-cc-pVDZ at C_{2v} symmetry. These calculations show that X band corresponds to electron ejection from the σ character highest-occupied molecular orbital (HOMO) of phenide, while the A band corresponds to the π HOMO-1. These Hartree-Fock (HF) orbitals are shown in Figure 4.2.

The mode frequencies and symmetries of phenide, σ-phenyl, and π-phenyl are shown in Table 4.1. Note that the standard Mulliken notation was used for all electronic and vibrational symmetry labels within the C_{2v} point group to be consistent with other previous work on phenide.[53, 65] Due to this notation, the π HOMO-1 shown in Figure 4.2 is transformed under the B_1 irreducible representation (B_1 and B_2 are switched in Q-Chem). When comparing Ph^- and π-Ph equilibrium structures, Ph^- geometry was optimized at CCSD (shown in Table 1 in the paper) and can be seen

mode number	Ph^- ($X\ ^1A_1$)		σ-Ph ($X\ ^2A_1$)		π-Ph ($A\ ^2B_1$)	
1	351	A_2	398	A_2	287	A_2
2	399	B_1	422	B_1	354	B_1
3	**591**	**A_1**	596	B_2	519	B_2
4	627	B_2	**616**	**A_1**	**579**	**A_1**
5	668	B_1	669	B_1	690	B_1
6	723	B_1	710	B_1	794	A_2
7	842	A_2	803	A_2	817	B_1
8	858	B_1	881	B_1	922	B_1
9	951	A_2	955	A_2	**924**	**A_1**
10	**958**	**A_1**	**980**	**A_1**	976	A_2
11	961	B_1	983	B_1	**991**	**A_1**
12	**1000**	**A_1**	**1017**	**A_1**	996	B_1
13	1041	B_2	1046	A_1	1016	A_1
14	1049	A_1	1069	B_2	1054	B_2
15	1143	B_2	1167	A_1	1103	B_2
16	1181	A_1	1167	B_2	1209	A_1
17	1270	B_2	1292	B_2	1254	B_2
18	1322	B_2	1334	B_2	1327	B_2
19	1412	B_2	1449	B_2	1383	B_2
20	1436	A_1	1458	A_1	1439	A_1
21	**1560**	**A_1**	**1572**	**A_1**	1533	B_2
22	1568	B_2	1630	B_2	**1626**	**A_1**
23	3017	A_1	3166	A_1	3173	A_1
24	3019	B_2	3171	B_2	3175	B_2
25	3065	A_1	3184	A_1	3193	A_1
26	3070	B_2	3186	B_2	3200	B_2
27	3134	A_1	3197	A_1	3215	A_1

Table 4.1: Harmonic frequencies (in cm^{-1}) and Symmetry Species of the Vibrational Normal Modes of Ph^-, σ-Ph, and π-Ph. B3LYP/aug-cc-pVDZ method was used for $Ph^-$and σ-Ph frequencies. EOM-IP-CCSD/aug-cc-pVDZ method was used for π-Ph frequencies. Standard Mulliken notation was used for the symmetry labels within the C_{2v} point group to be consistent with other previous work on phenide.[53, 65] The bolded numbers in the table correspond the normal modes in Figure 5 of the published paper as well as Figure 4.3 in this chapter.[49]

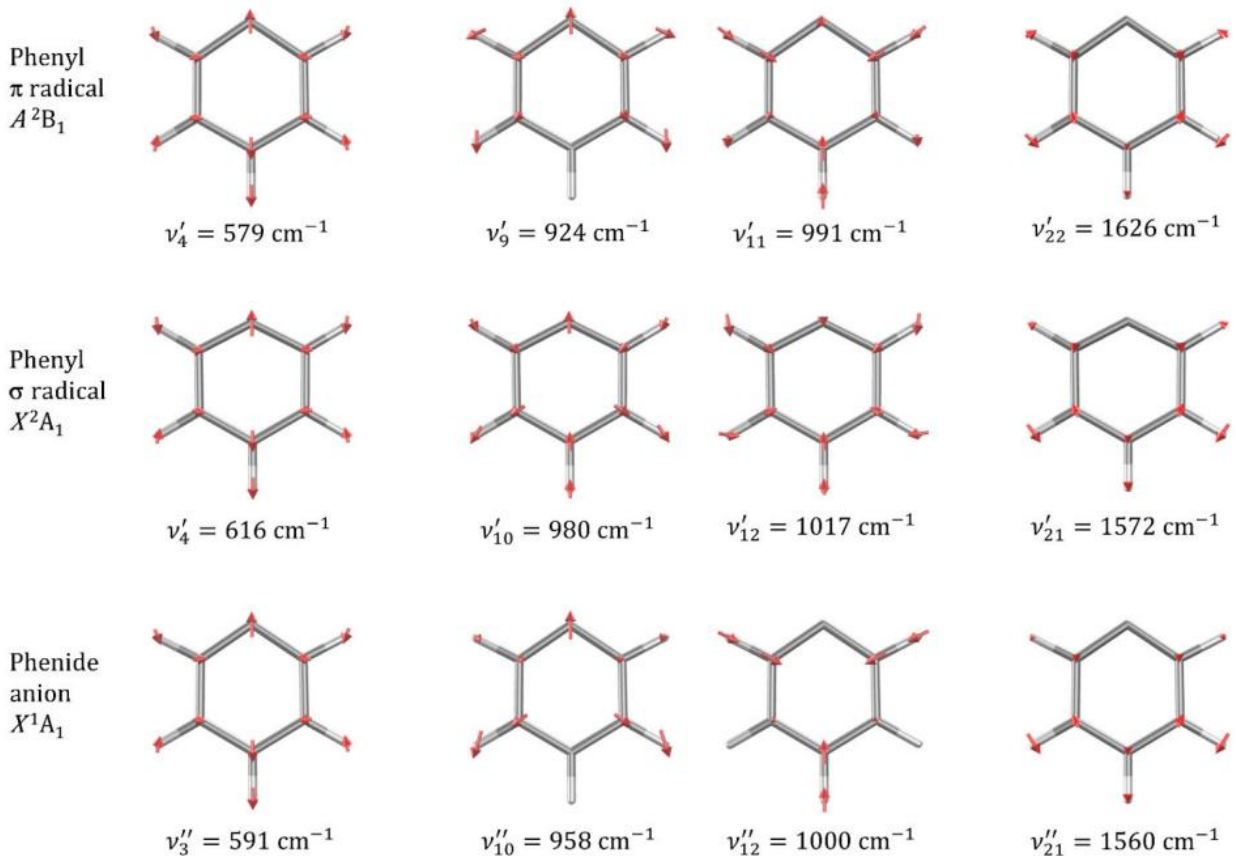

Figure 4.3: Fundamental frequencies and coordinates for phenide, σ-phenyl, and π-phenyl. Several normal vibrational modes, including FC-active spaces, are represented for (top) π-phenyl, (middle) σ-phenyl, and (bottom) phenide. These modes are bolded in Table 4.1.

in Figure 4.3.[49] These vibrational modes listed in Figure 4.3 are also bolded in Table 4.1 as these modes correspond to normal modes. The notations for the frequencies and vibrational modes of the target neutral (Ph) and initial anion (Ph^-) are represented as v_i' and v_i'', respectively. The index for the vibrational modes (1 – 27) is listed as i' for the target and $i''$for the initial. The normal modes of the anion and the neutral are not generally identical. For example, the v_4' mode of σ-Ph is closely resembled to the v_3'' mode of π-Ph. More modes that closely resembled to each other are shown in Figure 4.3.

4.4 Discussion

4.4.1 General Franck-Condon Simulations

The FC factors are calculated using the program ezFCF developed by Gozem and Krylov.[20] Harmonic frequency inputs used for this program were obtained from Table 4.1. The FC factors obtained helped produce the FC spectral simulations that will be presented throughout this Section. All the runs that were attempted or estimated are represented in Table 4.2. For the calculated FC factors, the parallel normal-mode approximation was used; however, the results of this approximation were also compared to the spectra obtained under the Duschinsky rotations of the normal modes. The two approaches resulted in similar spectra.

To compare to the experimental spectra, we generated model spectra by multiplying the transition intensities by the corresponding Boltzmann factors, $e^{-E''/kT}$, where E'' is the initial-state (anion) vibrational excitation energy. The raw FC spectra were then scaled by a Wigner-like function to account for electronic cross-section's eKE dependence: $f_w(\mathrm{eKE}) = \mathrm{eKE}^P$ where P = ½. This value is commonly used for a zero-dipole s wave emission only but can be used for a relatively small dipole moment like phenyl. Using the B3LYP method, the dipole moment of σ-

Run	Modes included	Max excitations Anion	Max excitations Neutral	Vibrational states Anion	Vibrational states Neutral	No. of comb. bands	Apprx. time[a]
X1	27 (all)	24	24	6.26×10^{9}	6.26×10^{9}	3.92×10^{19}	8×10^{6} yrs
X2	27 (all)	10	10	3.48×10^{8}	3.48×10^{8}	1.21×10^{17}	25,000 yrs
X3	27 (all)	0	10	1	3.48×10^{8}	3.48×10^{8}	40 min
X4	10 (all A_1)	0	16	1	5.31×10^{6}	5.31×10^{6}	<1 min
X5	3 ($\mathbf{Q}_X^3$)	24	24	2925	2925	8.56×10^{6}	<1 min
X6	2 (ν'_4, ν'_{10})	24	24	325	325	1.06×10^{5}	1 sec
A1	27 (all)	0	4	1	31465	31465	<1 sec
A2	3 ($\mathbf{Q}_A^3$)	24	24	2925	2925	8.56×10^{6}	<1 min
A3	3 ($\mathbf{Q}_A^3$)	8	8	165	165	27225	<1 sec

[a] The calculations were carried out on an Intel Core i7-7700HQ 2.80 GHz processor using 16 GB of RAM.

Table 4.2: FC factor calculations using ezFCF for Ph^-. This lists the completed or attempted calculations with computation time. Note that run X2 shows that if all modes were included with 24 significant excitations in both the anion and neutral that the approximate time would be 8×10^6 years, while run X5 only considers 3 important active modes with 24 significant excitations in both the anion and neutral to result in less than a minute in computation time. Further discussion will be in Section 4.4.2.

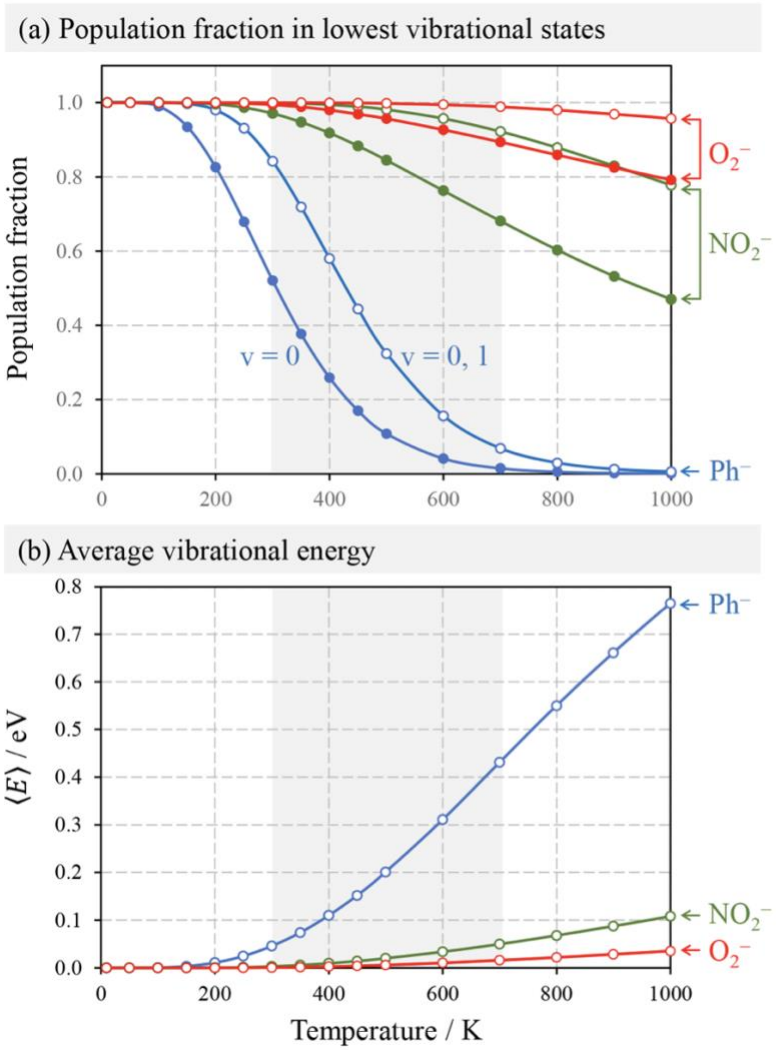

Figure 4.4: Temperature-dependent statistical comparison of Ph^-, O_2^-, and NO_2^-. The shaded region on the graphs represents the temperature range of 300 – 700 K. (a) The population fraction in the lowest vibrational states for Ph^- (blue), O_2^- (red), and NO_2^- (green) for the temperatures between 0 – 1000 K. The filled circle is for the fractional population of the ground vibration state, v = 0. The unfilled circle is for the combined fractional population of the ground state and singly excited states, v = 0, 1. (b) The average vibrational energy, $\langle E \rangle$, for Ph^- (blue), O_2^- (red), and NO_2^- (green) for the temperatures between 0 – 1000 K.

Ph was 0.87 D. Furthermore, to account for experimental broadening, the FC stick spectrum was convoluted with a Gaussian function. The broadening width was assumed to be dependent of the electron kinetic energy (eKE). The full width at half-maximum was defined as $w_0\sqrt{\text{eKE}}$, where $w_0 = \sim 0.02\ \text{eV}^{1/2}$.

4.4.2 Statistical Simulation of Hot Phenide

As mentioned earlier in this chapter, the method used to analyze the energy spectrum of hot phenide requires statistical methods. Figure 4.4 illustrates how the vibrational population of polyatomic ion, Ph^-, are affected by temperature compared to simpler species like O_2^- and NO_2^-. The congested photoelectron spectra of hot phenide are due to the contribution of the many distinct vibrational transitions. FC factor estimated times were listed along with modes and excitations are shown in Table 4.2. Phenide has 27 vibrational modes (3N – 6 with N = 11 atoms). Starting with the first run, X1, this run encompasses all 27 vibrational modes of phenide. The max excitation used here for both the anion and neutral is 24 each. The number of vibrational states for the anion is 6.26×10^9 as well as the neutral. This yielded an approximated time of 8×10^6 years to compute at these given parameters. This is an unfeasible amount of time. Considering all 27 modes included and lowering the number of max excitations in the anion and neutral to 10 each, lowered the approximate time significantly however 25000 years is still an unreasonable amount.

Runs X3 shows how cold phenide, with all 27 modes, is drastically shorter to compute compared to its hot counterpart. This is due to the max excitation for the anion at 0, making the approximate time to 40 minutes. Run X4 (active modes only) shows a reasonable computation time for cold anion at ground state (max excitations for anions = 0) to excited neutral states (max excitations for neutral = 16). However, by only considering some vibrational modes (runs X5 and

X6), then a reasonable time to compute is shown for considering max excitations in the anion and neutral (<1 minute and 1 second, respectively). The important vibrational modes that are used for runs X5 and X6 will soon be discussed. Ultimately, the FC factors and statistical simulation used help determine the temperature of hot phenide with computation time in mind.

Careful considerations of which vibrational modes were used for the FC simulation. The X band can be represented by two σ-Ph active modes: the v_4' and v_{10}'; however, the spectrum was improved significantly when another mode, v_{12}', was added to the calculations. Therefore, it was best determined that for $\mathbf{Q}_{\mathrm{X}}^{3}$ (run X5) v_4', v_{10}', and v_{12}' modes were used only to produce the best FC simulation for the X band. The FC-active space $\mathbf{Q}_{\mathrm{X}}^{3} \equiv \{v_3'', v_{10}'', v_{12}''\} \approx \{v_4', v_{10}', v_{12}'\}$. Superscript 3 represents the space's dimensionality and X refers to the X band. Three π-Ph modes can represent the A band: v_4', v_9', and v_{22}'. This gives the best FC-active space of the A band, $\mathbf{Q}_{\mathrm{A}}^{3} \equiv \{v_3'', v_{10}'', v_{21}''\} \approx \{v_4', v_9', v_{22}'\}$. Here, the superscript 3 still represents the space's dimensionality and the A refers to the A band. All vibrational modes were compared to Lineberger and Sivaranjana Reddy et al. to confirm that the frequencies matched theirs.[53, 65]

4.4.3 Dark-Bath Model and Bright-Bath Model on Phenide

The results of the dark-bath model for phenide can be found in Figure 9 and Figure 10 of the paper.[49] The "bath" is defined by the coordinates of the 24 FC-inactive modes with the 3 FC-active modes treated separately. For the X band, $\mathbf{B}_{\mathrm{X}}^{24}$ excluded the v_3'', v_{10}'', and v_{12}'' and for the A band, $\mathbf{B}_{\mathrm{A}}^{24}$ excluded v_3'', v_{10}'', and v_{21}'' modes. The dark bath model assumed that FC-active modes are responsible for all observed transition intensities for hot phenide. The dark bath accounts only for the degeneracy for each active-space state. Overall, the dark-bath model showed similarities to the isolated FC-active space method. This is not surprising, as both models relied on the FC-active

model	X band[a] (K)	A band (K)
FC active modes only	3400	3400
	3000	
	3000	
FC active modes + dark bath	3400	3400
	3000	
	3000	
FC active modes + bright bath	750	750
	620	
	600	
energy conservation	700	500
	700	
	700	

[a]The three values listed are for the 355, 532, and 611 nm spectra, respectively, for each corresponding model.

Table 4.3: Temperatures based off different models for hot phenide. Four models were used to understand the temperature of the experimental spectra: FC active modes only, dark-bath, bright-bath, and the energy conservation model. The latter presented the best agreement to the experimental spectra of hot phenide at 700 K.

space for spectral intensities. The main difference between the two was that the isolated model did not consider FC inactive vibrations, while the dark-bath model only considered the degeneracies from inactive modes. However, both models showed unrealistic temperatures >3000 K (see Table 4.3).

In the bright-bath model for phenide, the bath modes mentioned earlier are assumed to have some contributions towards the spectral intensities, borrowing these intensities from degenerate active space states. When the bright-bath model is compared to the dark-bath and isolated FC-active space model, the bright-bath model is several folds lower in temperature. The temperatures of these modes can be found in Table 4.3. Although the bright-bath model shows a realistic ion temperature compared to the other two previous models, the bright- bath model overestimates the higher eBE transitions from the lower energy anion to the excited states of the neutral. Therefore, a better model is still needed.

4.4.4 Energy Conservation Model for Phenide

As the name suggests, the energy conservation model is based solely off the conservation of energy. The idea behind this approach is shown in Figure 4.5. What this scheme depicts is how transitions between the ground state of the anion to the neutral and transitions between the excited state of the anion to the neutral can alter the photoelectron spectrum differently. A linear transformation of the ground state spectrum is used to predict the excited state spectrum. The cold ground state spectrum of phenide is obtained from the previous calculations of the FC simulation. From there, the spectrum is transformed to the excited state spectrum. We set an anchor point that is just to the right of the transition's VDE. The $S_0(\mathrm{eBE})$ has an eBE = electron affinity (EA) which is altered until it matches the spectrum of $S_{E''}(\mathrm{eBE})$ eBE = EA– *E''*. To simplify, imagine the blue

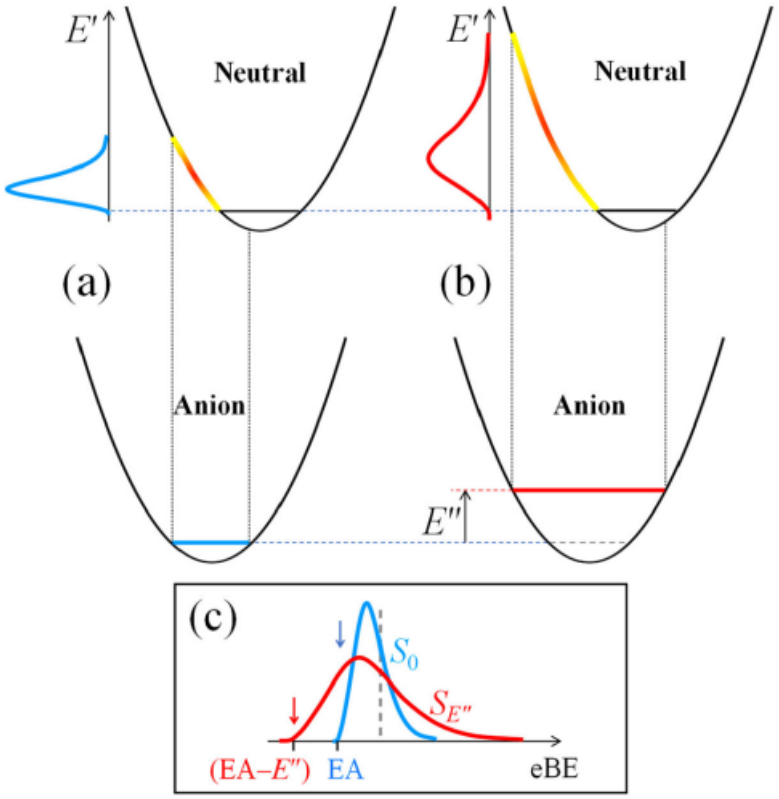

Figure 4.5: Schematic model based off the conservation of energy. This schematic shows the comparison between the transition from a ground state anion and the transitions from an excited state anion. (a) The transition between the ground state of the cold anion to excited states of the neutral with a blue energy spectrum on the left. (b) The transition between the excited states of the anion to excited states of the neutral with a red energy spectrum on the left. The accessed regions of the neutral are colored by a gradient. (c) The two energy spectrums are compared to each other. The red spectrum is shifted to the left (EA – *E''*). The energy conservation model transforms $S_0(\text{eBE}) \rightarrow S_{E''}(\text{eBE})$ with an anchor (blue dashed line) to the right of the VDE. This will alter the eBE = EA of $S_0(\text{eBE})$ to eBE = EA– *E''* of $S_{E''}(\text{eBE})$.

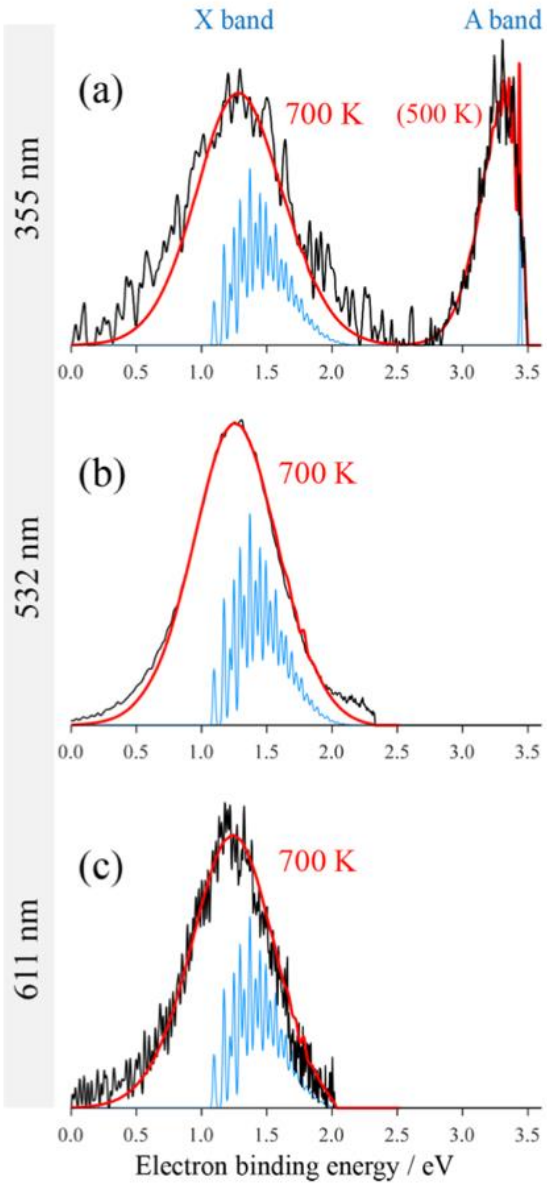

Figure 4.6: The energy conservation model compared to the experimental spectra of hot phenide. The model, in red, is compared to obtained spectra at (a) 355 nm, (b) 532 nm, and (c) 611 nm which is represented in black. The light blue is the FC reference spectra at T = 0 (runs X3 and A1).

spectrum as a rubber band and is tied down by the anchor. The left side is stretched to the red spectrum's left side, as well as the right side, while keeping the normalization. This is stretched until the blue spectrum is now the red spectrum. Further details are discussed in the paper.

The results of the energy conservation model are shown in Figure 4.6. The model estimates that the temperature of hot phenide is ~700 K. It is noted that the A band in 355 nm spectrum has a temperature of 500 K. As stated before, the two detachment orbitals, σ and π, corresponds to the X and A band, respectively. The X band transition involves a more geometry change of Ph^- to Ph, making the X band in the spectrum broader. Unfortunately, this model overestimates the bandwidth for a given temperature and underestimates the temperature for a given bandwidth. This means that the temperature of 700 K at the X band is more reliable than 500 K at the A band; therefore, 700 K is the approximate temperature to describe the experimental phenide temperature.

4.5 Conclusion

The focus of this chapter was to highlight the importance of using a statistical approach rather than a state-specific approach to analyze hot polyatomic ions that are congested. The paper accounts for a greater in-depth detail about these models used to determine the temperatures of highly congested and broad spectra of hot ions, specifically phenide. As mentioned, congested spectra cannot be analyzed using the complete FC calculations, thus several models have been determined using limited FC analysis and statistical calculations. The models that were used to analyze phenide was the isolated FC active modes, dark-bath model, bright-bath model, and the energy conservation model.

The isolated FC active modes and dark-bath model are like each other and resulted in similar temperature values for each wavelength measure. The bright-bath model has a more

realistic ion temperature but overestimates contributions of the higher eBE transitions from the low energy states of the anion to the excited states of the neutral. The energy conservation model uses a linear transformation of the ground spectrum of the anion to predict the excited states, giving a temperature of 700 K for phenide. The temperatures associated with each model are listed in Table 4.3. for 355 nm (3.49 eV), 532 nm (2.33 eV), and 611 nm (2.03 eV). This method is an efficient way for tethering limited state-specific quantum calculations with statistical analysis to understand photoelectron spectra of hot ions.

Chapter 5: Microhydration of Hot Phenide: Photoelectron Spectroscopy and Statistical Mechanics

Further diving into understanding hot ions introduces the idea of microhydration. This chapter peers into the understanding of how one and two water molecules affect the phenide ion ($C_6H_5^-$ or abbrev. Ph^-). In Chapter 4, the experimental temperature of phenide was approximately 700 K, which resulted in a highly congested and convoluted photoelectron energy spectrum. The main purpose of this present chapter is to study the spectroscopy of phenide clusters and understand the statistical mechanics of microhydration at high temperatures. To understand the stability and limit of the thermal excitation the phenide-water interaction at high temperatures can withstand, the thermodynamics of the solvation needs to be examined. In our paper, we define characteristic solvation temperature (CST) as the upper limit of the temperature that the clusters can sustain.[66] For example, the initial hot cluster ions are cooled *via* evaporative cooling as it reaches the CST according to their microsolvation interactions. The temperature of Ph^-H_2O and $Ph^-(H_2O)_2$ was approximately 560 K and 520 K, respectively.

This chapter is divided into several sections. Section 5.1 discusses the importance of solvation in clusters. The importance of studying hot ions was already mentioned in Chapter 4. Section 5.2 briefly touches on the experimental methods of this project as it is similar to the previous chapter. The experimental results and analysis are mentioned in Section 5.3. This section also describes the parameters used to analyze the data using the Wigner-like function mentioned in Chapter 4. The modeling of phenide with water as well as the discussion is in Section 5.4. Lastly, the conclusion of the experiment and findings are in Section 5.5. This chapter provides the importance of microhydration and does not go into depth of the details of the mathematical aspects (which can be found in the paper).[66]

5.1 Importance of Solvation

Solvation is important to study due to it being a common manifestation of intermolecular (IM) interactions. Commonly, solvation of a core anion lowers the energy and stabilizes the core anion.[67-69] As each sequential solvent is added to the cluster, the solvent will have a less of a stabilizing effect on the core anion, eventually saturating it. As expected, this stabilization effect and hydration shift is shown in this experiment with H_2O on Ph^-, which will be discussed more in Section 5.3. The importance of hot ions and phenide was described earlier in Section 4.1, which explained how phenide is an important intermediate of PAHs ranging from combustion reactions to atmospheric chemistry. The relatively cold spectrum of phenide of ~300 K was investigated by Lineberger and co-workers.[65]

While the previous chapter looked at the hot spectrum of phenide at ~700 K and the IM motions of the ion, this study focuses on the IM motions between phenide and water as this is the contributing factor towards the cluster's statistical properties. For example, at 0.5 eV excitation for Ph^-H_2O, there are 24,867 accessible internal states for Ph^-, but 248,525 interaction states for Ph^-H_2O. These IM degrees of freedom contribute to how much thermal excitation the cluster can withstand, which can be seen through evaporative-cooling or Ar-tagging.[70-74] Aside from evaporative-cooling, as stated earlier, what is focused in this study is understanding the strength and stability of microhydrations (e.g., H_2O) on these clusters at high temperatures. Water can also be seen as a tag but has a larger binding energy compared to argon. Furthermore, the microhydration strength of water can create a relatively stable cluster at high temperatures without immediate predissociation, unlike argon. The thermal excitation limit between the interaction of phenide-water is determined by the thermodynamics solvation or, as we have defined, the CST. When the source temperature is greater than the CST, the initial hot cluster ions are cooled through

solvent evaporation until the ion reaches the CST. In this situation, the temperature of the hot ions is not determined by the source temperature, but by the microsolvation interactions. Unlike the "hot" source (source temperature > CST), the "cold" source (source temperature < CST) determines the temperature of the initial ions. The possibility of controlling the temperature of ions have been discussed in Section 2.6.

5.2 Experimental Methods

The same methods were used for this experiment as in Section 4.2. The precursor was benzeneselenol (C_6H_5SeH or PhSeH) with traces of water using argon as the carrier gas at a backing pressure of ~1.8 atm. The electron cannon set-up was used in this experiment. The electron source is positioned close to the nozzle, like the previous experiment in Chapter 4. The electron beam interacts with the supersonic expansion from the nozzle to generate hot plasma. Due to this set-up, there is a smaller chance for collisional cooling of the ions; therefore, this set-up increases the presence of hot ions. Ions are separated by mass in time in the Wiley-McLauren TOF mass spectrometer that is discussed in Section 2.3.[13] Once the ion of interest is found (Ph^-, Ph^-H_2O, and $Ph^-(H_2O)_2$), the ions are intersected by a pulsed laser beam. From a Spectra Physics Lab- 130-50 Nd:YAG laser at a repetition rate of 50 Hz, 532 nm and 355 nm was produced as a second and third harmonic, respectively, while Rhodamine 640 dye in a ND6000 dye laser was used to produce the 611 nm light. More information about laser specifications is described in Section 2.4. A VMI assembly along with a positive-sensitive dual microchannel-plate imaging detector coupled with a P47 phosphor screen was used. The photoelectron images were captured using a charge-coupled device camera (Roper Scientific, Inc.). The photoelectron energy spectrum was obtained using inverse Abel transformations and the BASEX program on the collected images.[16-17]

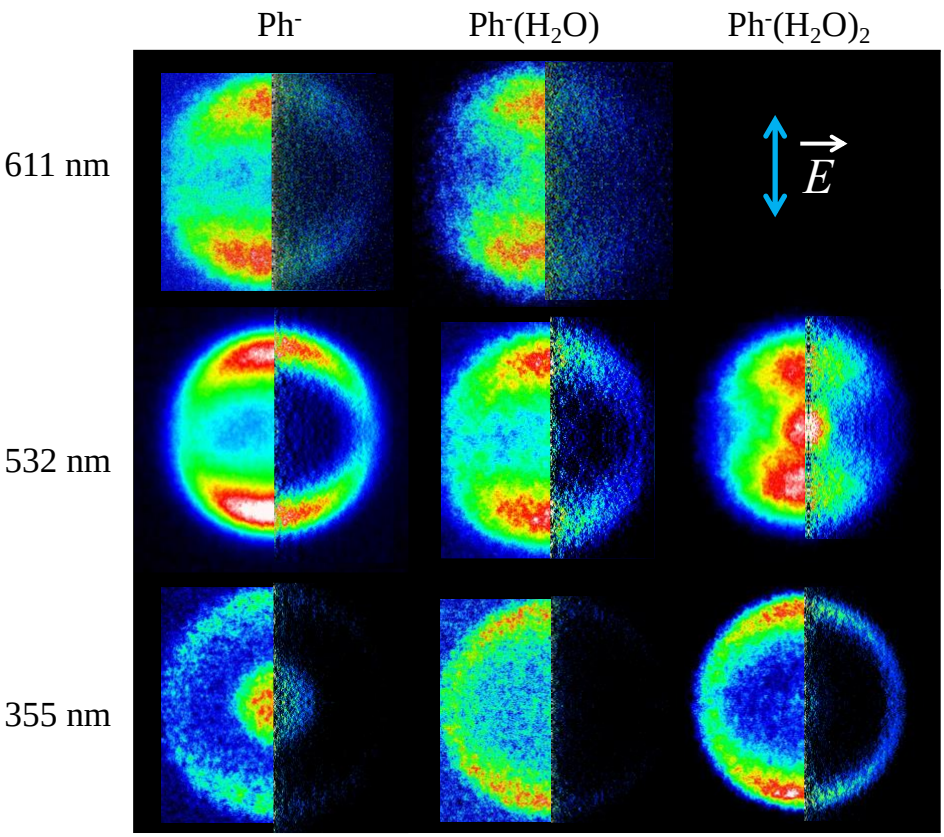

Figure 5.1: Photoelectron images of Ph^-, Ph^-H_2O, and $Ph^-(H_2O)_2$. The raw photoelectron images are shown on the left half and the inverse Abel transformation on the right half. Ph^- and Ph^-H_2O images were obtained at 355 nm (3.49 eV), 532 nm (2.33 eV), and 611 nm (2.03 eV), while $Ph^-(H_2O)_2$ images were obtained at 355 nm and 532 nm. The polarization of the laser is noted at the top-right corner of the figure.

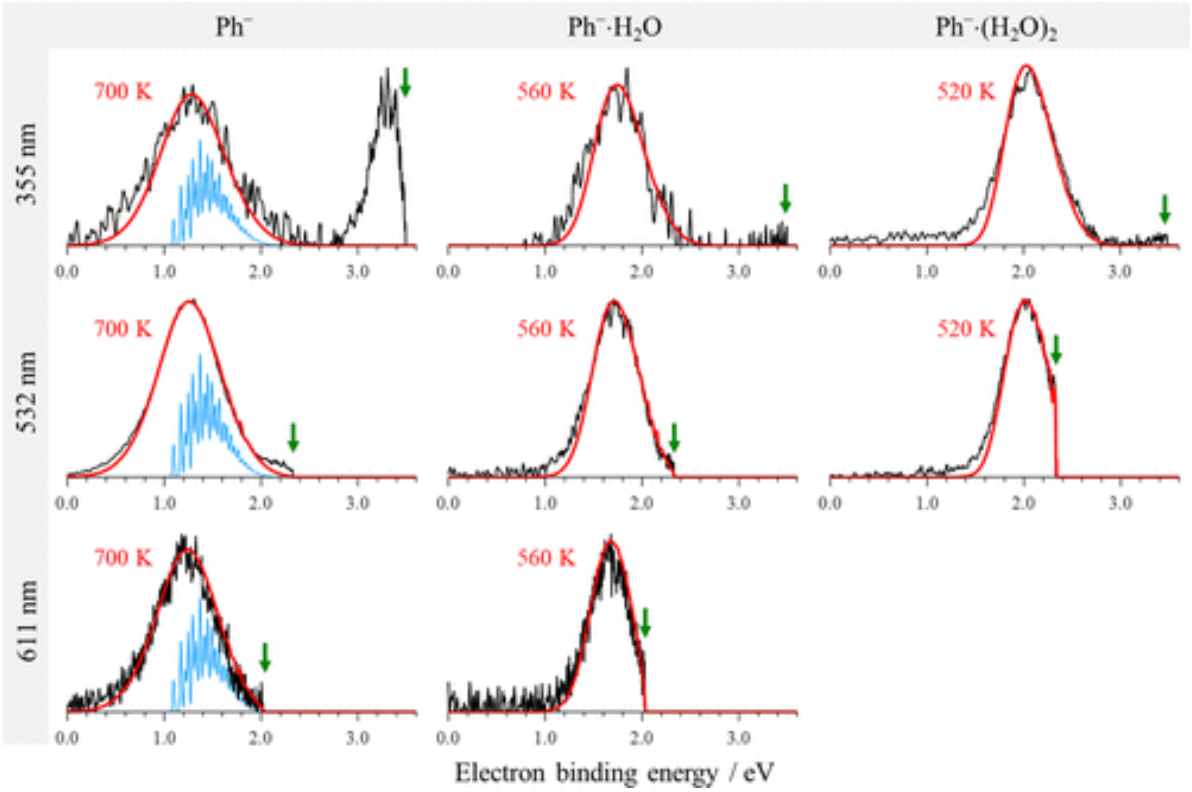

Figure 5.2: Photoelectron energy spectrum of Ph^-, Ph^-H_2O, and $Ph^-(H_2O)_2$. Ph^- and Ph^-H_2O were measured at 355 nm, 532 nm, and 611 nm, while $Ph^-(H_2O)_2$ were measured at 355 nm and 532 nm. The experimental data is represented by the black lines, the modeled spectra is represented by the red lines with the temperature indicated nearby, and the FC simulation is in blue. The spectra are plotted with respect to the electron binding energy. The energetic limit is indicated by green arrows in each spectrum. The solvated phenide species have spectrums that are shifted to the right towards larger eBE due to the stabilization of the core phenide by water.

5.3 Experimental Results and Analysis

The photoelectron images of Ph^- and Ph^-H_2O were obtained at 355 nm (3.49 eV), 532 nm (2.33 eV), and 611 nm (2.03 eV), while images of $Ph^-(H_2O)_2$ were obtained at 355 nm and 532 nm. The raw photoelectron and inverse Abel transformation images of phenide and phenide with water can be seen in Figure 5.1 on the left and right side, respectively. The light polarization is indicated on the top-right corner of the figure. All images except for Ph^- at 355 nm have a single broad electronic band that corresponds to the photodetachment of the ground electronic state from $Ph^-$to σ-Ph. The second electronic band that is present in Ph^- at 355 nm corresponds to the first excited state of phenyl or π-Ph. In this chapter, the focus is the micohydration-induced changes occurring in the σ-Ph transition.

The energy spectrum for these photoelectron images (from Figure 5.1) is shown in Figure 5.2. The experimental data is represented in black and compared to the modeled spectrum in red and FC simulation in blue. These spectra are plotted with respect to the electron binding energy (eBE). The green arrows on each spectrum indicate the energetic limit, $\text{eBE} = h\nu$. All temperatures are indicated in the figure that were determined by the modeled spectrum in red. The modeling used for Ph^-H_2O and $Ph^-(H_2O)_2$ is similar to the model discussed in Chapter 4 for Ph^-. The energy conservation model, mentioned in Chapter 4, was used for the analysis of the experimental data. The state-specific approach cannot be used here is the same reason that it could not be used for phenide due to thermal excitations. Furthermore, the additional IM degrees of freedom from phenide-water cluster increases the complication of the FC analysis as explained earlier.

Ph^-H_2O and $Ph^-(H_2O)_2$ follow similar trends of other clusters, where the addition of a solvent stabilizes the energy of the core.[67-69] The stabilization effect of the solvent on the core anion is referred to as the hydration shift (HS). This effect is shown in Figure 5.2 with the vertical

species	T/K	Wigner exponent	hydration shift/eV
Ph^-	700(10)	0.50	0
$Ph^-\cdot H_2O$	560(10)	0.45	0.38(1)
$Ph^-\cdot(H_2O)_2$	520(10)	0.10	0.63(1)

Table 5.1: Summary of parameter values used to produce the model spectra for Ph^-, Ph^-H_2O, and $Ph^-(H_2O)_2$. The model used here is the energy conservation model that was described in Chapter 4 and was initially used for phenide. This model spectra is reflected in Figure 5.2 in red.

detachment energy (VDE) is shifted to the right or to higher eBE with each additional water molecule. The VDE was discussed in Section 1.3. With one water molecule, the HS = 0.38 eV for $Ph^{-}H_2O$ and with two water molecules the HS = 0.63 eV for $Ph^{-}(H_2O)_2$ when compared to Ph^{-} alone (HS = 0). Both solvated species, $Ph^{-}H_2O$ and $Ph^{-}(H_2O)_2$, have a slightly narrower spectrum when compared to the unsolvated phenide, Ph^{-}.

The vibrational envelope of the model spectrum was scaled by an appropriate Wigner-like function ε^P, where $\varepsilon \equiv$ eKE $= h\nu -$ eBE, accounting for the eKE-dependence of the electronic part of the photodetachment cross section.[75-77] Generally, the Wigner exponent controls the rise of the spectral intensity from zero near eBE $= h\nu$, which are indicated by the green arrows in Figure 5.2. A *s* wave emission with little to no dipole moment of the neutral can be described by a Wigner exponent of P = ½. For a large-dipole field, the Wigner exponent P values may need to be smaller.[18, 76] The square root scaling (P = ½) did not match several of the spectra at the low-eKE behavior. Therefore, lower P values were needed to model the experimental data. A slightly lower P value of 0.45 was used to model $Ph^{-}H_2O$. The lower P value of 0.10 used for $Ph^{-}(H_2O)_2$ at 532 nm was required to reproduce the same increase on the left side of the eBE $= h\nu$ (indicated by the arrow). For this experiment, Ph^{-} has a Wigner exponent P = 0.50, $Ph^{-}H_2O$ has a P = 0.45, and $Ph^{-}(H_2O)_2$ has a P = 0.10. The value of P is physically determined by the dipole moment of the neutral residue and can be assigned to the same P value at different wavelengths of each species.

The spectral modeling used two assumptions: (1) the temperature of solvated phenide will generally differ from unsolvated phenide and (2) there is a HS that stabilizes phenide when water is introduced. The different wavelength of 355 nm, 532 nm, and 611 nm for each species use the same parameters of T, HS, and the Wigner exponent due to being independent of the photon energy. All the parameters used for the model spectra has been summarized in Table 5.1.

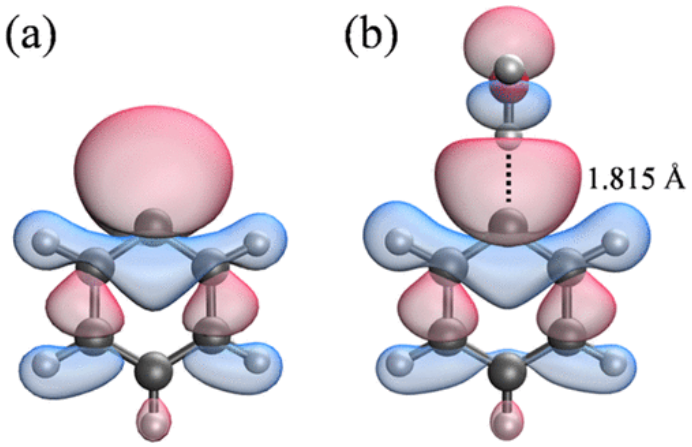

Figure 5.3: Hartree-Fock HOMOs of phenide and phenide-water cluster. (a) Phenide has a C_{2v} point group and (b) $Ph^{-}H_2O$ has a C_s point group. The distance between phenide and the water molecule was 1.815 Å. Both were calculated using the CCSD level of theory with the aug-cc-pVDZ basis set. The isovalues used was 0.05. The vibrational frequencies for both species are listed in the SI of the paper.[66]

5.4 Modeling and Discussion

5.4.1 Ab Initio Calculations

The geometry and frequencies of Ph^- and Ph^-H_2O were calculated at the level of theory and basis set of CCSD/aug-cc-pVDZ using Q-Chem 5.1 program.[19-20] The optimized closed-shell electron configuration of phenide has a point group of C_{2v}, and Ph^-H_2O has a point group of C_s. The HF HOMOs of phenide and phenide-water cluster can be seen in Figure 5.3, which is an electron detachment from the σ-Ph transistion. The geometry parameters and vibrational frequencies of both ions can be found in the SI of the paper.[66] The water molecule on phenide in (b) of Figure 5.3 is perpendicular to the plane of the phenide molecule. Additionally, other geometries were considered (not shown) for Ph^-H_2O, including water in-plane with phenide that resulted in a higher energy or less stable by 0.012 eV. The calculated dipole moment of both phenide and phenide-water cluster was 0.88 Debye and 3.33 Debye, respectively. $Ph^-(H_2O)_2$ calculation has not been attempted, but the dipole moment is assumed to be larger. The dipole moment trend presented here correlates to the Wigner exponent trend, where a larger dipole moment requires a smaller Wigner exponent to model the spectrum. It is assumed that these calculations can be extended to $Ph^-(H_2O)_2$ as well.

A one common way to understand the effects of microhydration is to look at the VDE, which is described in detail in Section 1.3. The VDE is calculated by the difference between the energies of the neutral species at the optimized anion geometry and the optimized anion. The calculated VDEs of phenide and Ph^-H_2O were 1.432 eV and 2.205 eV, respectively. This was at CCSD level of theory and aug-cc-pVDZ basis set. The hydration-induced VDE shift between the two is $\Delta VDE = Ph^-H_2O - Ph^- = 2.205\ eV - 1.432\ eV = 0.774\ eV$. However, the experimental HS = 0.38 eV between hot-ions Ph^- and Ph^-H_2O. Although it may see surprising at first to see a drastic

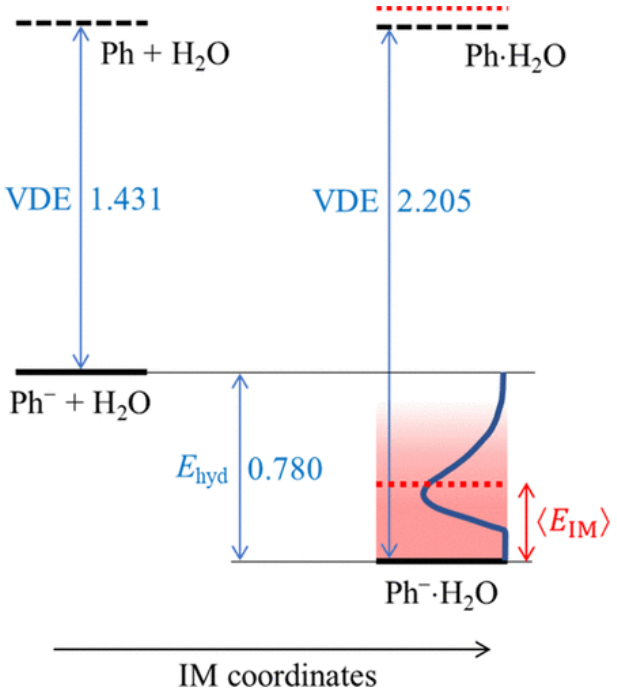

Figure 5.4: Energy diagram schematic of Ph^- and Ph^-H_2O photodetachment. The VDE for Ph^- and Ph is 1.431 eV, while the VDE between Ph^-H_2O and Ph H_2O is 2.205 eV. The calculated VDE = 1.431 eV and 2.205 eV corresponds to Ph^- and Ph^-H_2O, respectively. The corrected calculated hydration energy was found to be at $E_{\mathrm{hyd}} = 0.780$ eV. The black dashed lines correspond to the neutral molecules at their respective optimized anion geometry. The red dashed lines refer to the neutral state excitation from 40% of $\langle E_{\mathrm{IM}} \rangle = 0.13$ eV.

difference between the hydration-induced VDE and HS, the prior hydration shift calculation is applicable only at ground state (i.e., cold ion only), while the HS includes thermal excitations above the ground state of the anion.

Another approach was used to look at the energetic effect of hydration by combining the separate energies of Ph^- and H_2O, then subtracting the energy of Ph^-H_2O: $E_{\mathrm{hyd}} = E(\mathrm{Ph}^-) + E(\mathrm{H_2O}) - E(\mathrm{Ph}^-\mathrm{H_2O})$. The CCSD calculated energy resulted in $E_{\mathrm{hyd}} = 0.849$ eV, an overestimation due to the basis set superposition error (BSSE). BSSE occurs when more basis function is used than needed. This was fixed by calculating the counterpoise correction for Ph^- and H_2O energies with the same basis sets for Ph^-H_2O.[78] The details of the calculated correction is explained more in the paper. The corrected hydration energy was $E_{\mathrm{hyd}} = 0.780$ eV. This hydration energy is closer to the calculated ΔVDE = 0.774 eV and smaller than the incorrected estimated $E_{\mathrm{hyd}} = 0.849$ eV. The minimal difference between the corrected E_{hyd} and ΔVDE is due to the neutral-state interactions. An energy diagram schematic for the photodetachment of Ph^- and Ph^-H_2O can be seen in Figure 5.4.

5.4.2 Understanding Microhydration

These *ab initio* ΔVDE and E_{hyd} should not be expected to match the experimental HS of the hot clusters as the first two, ΔVDE and E_{hyd}, expects the cluster to be at ground state or cold. However, most of phenide is already at the excited vibrational level at the temperature of 560 K for Ph^-H_2O. Using 3N – 6 (N = number of atoms) for nonlinear molecules, phenide has $3 \times 11 - 6 = 27$ vibration mode and water has $3 \times 3 - 6 = 3$ vibrational modes. Ph^-H_2O has $3 \times 14 - 6 = 36$ vibrational modes, which means 30 internal vibrational modes (from phenide and water) and 6 intermolecular (IM) modes between Ph^-H_2O. Generally, IM modes will have lower frequencies

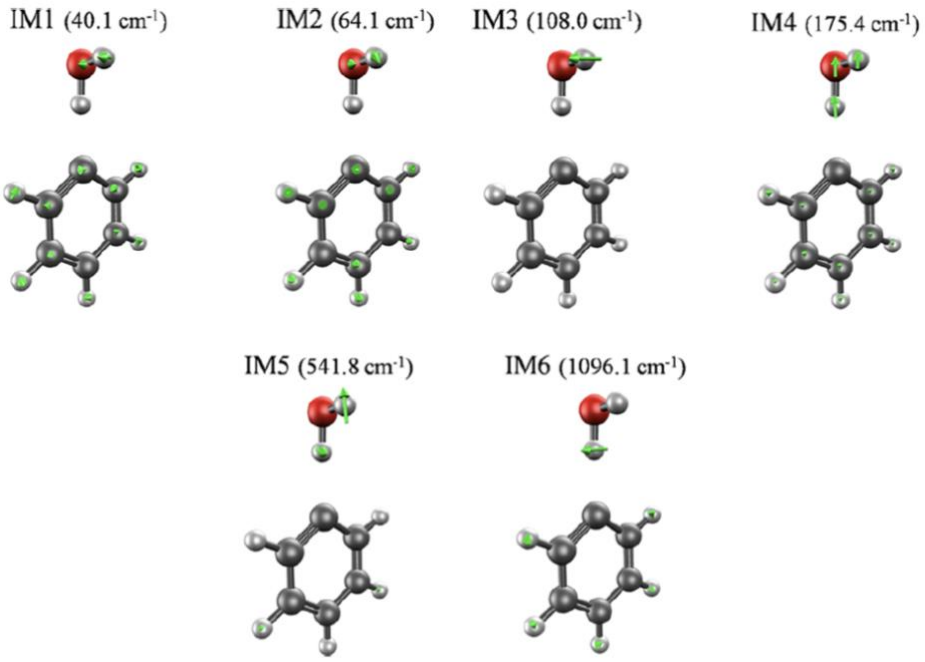

Figure 5.5: Vibrational modes and coordinates of $Ph^{-}H_2O$ corresponding to the phenide-water motions. Here, 6 vibrational modes are listed named IM1 – IM6 which corresponds to the 6 IM modes between phenide and water. The complete 36 vibrational frequencies are in the SI of the paper.[66]

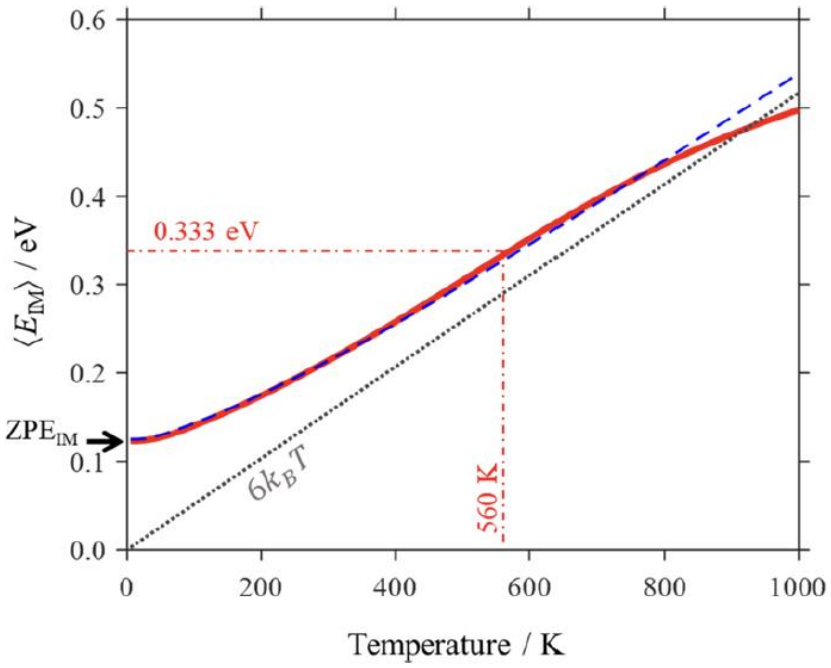

Figure 5.6: Calculated ensemble average of IM energy in Ph⁻H$_2$O as a function of temperature. The red curve is the ensemble average of IM energy in Ph⁻H$_2$O. The blue curve uses all six IM modes in the harmonic approximation. The black dotted line uses $\langle E_{\mathrm{IM}} \rangle = 6k_bT$ from the equipartition theorem at the classical harmonic limit. As temperature increases, the red curve starts to deviate at the $6k_bT$ limit and drops below both the quantum and classical harmonic limit. This is discussed more in Section 5.4.2 as well as in the paper.[66]

when compared to internal molecular vibrations and are more susceptible to finite temperatures. IM modes must be accounted for as it is absent in phenide alone when comparing the hydration shift, HS, to E_{hyd}. The associated average energy of intermolecular modes is described by $\langle E_{\mathrm{IM}} \rangle$ for $Ph^{-}H_2O$. Although both E_{hyd} and HS describe the cluster stabilization due to IM interactions, it is important to note that E_{hyd} is from the optimized $Ph^{-}H_2O$ geometry and HS considers a range of IM interactions of thermally averaged interactions.

Even at T = 0, correction needs to be made for the combined zero-point energies (ZPE) of the modes due to the range of the cluster geometries. To account for this, the 6 IM modes were represented by a six-dimensional oscillator canonical ensemble. The 6 IM modes are labeled IM1-IM6 and listed in Figure 5.5 and the full 36 vibrational frequencies for phenide-water can be found in the SI of the paper.[66] IM1, IM2, and IM4 were near the dissociation limit and IM3, IM5, and IM6 were responsible for hindered rotations. IM5 and IM6 also strongly coupled to the dissociation coordinates, while IM3 can be described as non-dissociative. Therefore, there are 5 modes that are dissociative: IM1, IM2, IM4, IM5, and IM6. More in-depth details are explained in the paper.[66]

The findings and results of this was the $\mathrm{ZPE_{IM}}$ = 0.123 eV. The IM excitation energy, E_{IM} – $\mathrm{ZPE_{IM}}$, is plotted in Figure 1 in the paper (not shown here). The model predicts that $\langle E_{\mathrm{IM}} \rangle$ = 0.333 eV at T = 560 K shown in Figure 5.6 by the red curve. This figure allows the comparison of the model with the equipartition theorem at the classical harmonic limit, where $\langle E_{\mathrm{IM}} \rangle = 6k_bT$ (1 k_bT/vibration). At low temperatures, the quantum model (blue dashed) deviates from the classical model (black dotted). The ensemble average (red solid) curve approaches the $6k_bT$ limit at high temperatures but does not completely become classical. Furthermore, this comparison shows how that anharmonicity is a major factor when T > 600 K due to the deviation and saturation of the ensemble average. The red curve drops below both the classical harmonic (black dotted) and the

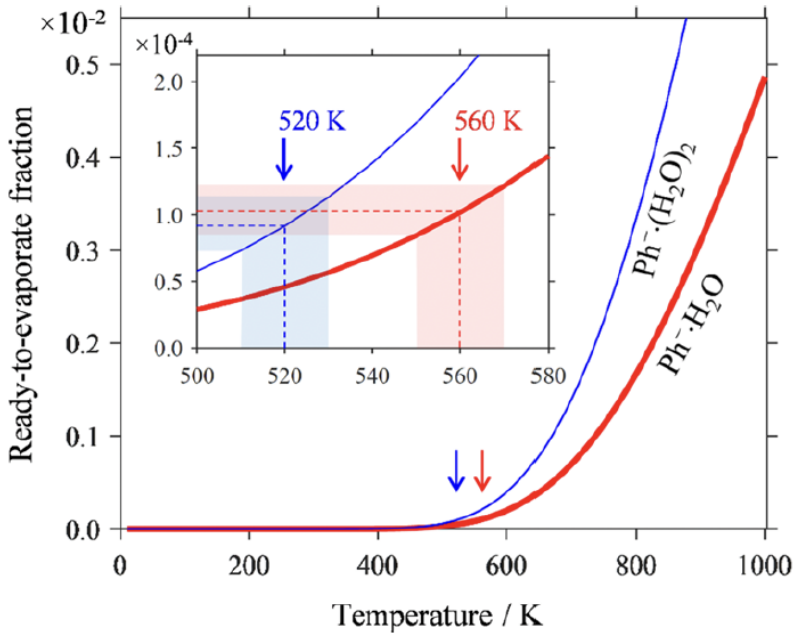

Figure 5.7: Ready-to-evaporate fraction as a function of temperature for $Ph^{-}H_2O$ and $Ph^{-}(H_2O)_2$. The red curve represents $Ph^{-}H_2O$ and the blue curve $Ph^{-}(H_2O)_2$. The blue and red shaded regions represent confidence intervals of $\pm$10 K for the uncertainties in RTE fractions.

quantum (blue dashed) line due to the Morse oscillator having a finite number of bound states and the E_{IM} maximum, where max $(E_{\mathrm{IM}}) = E_{hyd}$.[79]

5.4.3 Characteristic Solvation Temperature on Phenide-Water

The characteristic solvation temperature (CST) of a cluster is not determined by the ion source but is an intrinsic property of the microhydrations between the core and the solvated species. Here, the CST of $Ph^{-}H_2O$ was approximately 560 K shown in the IM energy distribution diagram (Figure 7 of the paper).[66] Furthermore, any T > 560 K results in dissociation of the cluster (e.g., evaporative cooling). The ready-to-evaporate (RTE) fractions is the 1% evaporation energy fraction of the cluster population having a total dissociative-mode energy (considering only the 5 dissociative IM modes):

$$f_{1\%} = P_5\left(E_{\mathrm{hyd}}\right)\Delta E_{\mathrm{IM}}^{(5)} \tag{5.1}$$

where $\Delta E_{\mathrm{IM}}^{(5)} = 0.01E_{\mathrm{hyd}}$. Due to the RTE fraction relating to the evaporation rate of the cluster, the RTE fraction tells us about the lifetime of the thermally excited cluster. For $Ph^{-}H_2O$, we have $P_5\left(E_{\mathrm{hyd}}\right) = 0.013$ eV^{-1} multiplied by $\Delta E_{\mathrm{IM}}^{(5)} = 0.01E_{\mathrm{hyd}} = 0.0078$ eV, gives $f_{1\%} = 1.0 \times 10^{-4}$ at 560 K. Resulting in 0.01% of $Ph^{-}H_2O$ as RTE. The $f_{1\%}(T)$ is shown in Figure 5.7 for both $Ph^{-}H_2O$ and $Ph^{-}(H_2O)_2$. What this shows is that at temperature lower than 500 K, the RTE fraction is almost zero, while just above 500 K, the RTE rises rapidly.

5.5 Conclusion

As mentioned earlier, the temperature of clusters is not always determined by the source temperature (e.g., electron cannon). With a "hot" source (source temperature > characteristic solvation temperature), the temperature of the cluster is controlled by the CST, an intrinsic

property of the cluster system. The limit is set by the solvent binding energy and the intermolecular degrees of freedom of the cluster. Therefore, the microscopic solvation determines the upper limit temperature of stable clusters. On the other hand, if the source temperature is lower than the CST, only then will the temperature of the ion will be determined by the source conditions and surroundings.

The CST of Ph^-H_2O and $Ph^-(H_2O)_2$ was 560 K and 520 K, respectively, with the same ion source as phenide (the temperature of phenide was around 700 K). Using the RTE approach, the estimated temperature for $Ph^-(H_2O)_3$ (not studied here) can be predicted to be around 500 – 505 K. Compared to the cold or ground state environment, the high temperature environment resulted in a decreased hydration stabilization effect and spectral band shifts. In general, the temperature of the CST of a cluster can be found using the inflection point of the $\langle E_{\mathrm{IM}} \rangle$ vs. T curve as shown in Figure 5.6 for Ph^-H_2O as an example.

Chapter 6. Summary and Future Directions

6.1 Summary

This dissertation described the different types of projects using photoelectron imaging spectroscopy. The first project (Chapter 3) showed how exit-channel interactions are not always negligible, i.e., the departing electron cannot be assumed to have no interactions with the neutral residue. SO^- provided the first extension for the dipole-field model from the detachment of a π^* orbitals. In the second project (Chapter 4), hot ions were investigated for the first time in the Sanov lab. This has opened new opportunities and pathways for studying hot ions as reactions in the universe are not necessarily cold or at room temperature. Lastly, the third project (Chapter 5) provided insights on microhydration interactions on hot clusters. Here, the temperatures of hot clusters were not determined by the source temperature, but by the characteristic solvation temperature. In all the projects, different computational methods were needed to fully understand and analyze the experimental data.

Chapter 3 focused on the experimental and theoretical photoelectron angular distributions (PADs) of sulfur monoxide anion. This experiment showed how the dipole moment of the neutral residue (e.g., SO) effects the PADs. The common methods of *ab initio* calculations could not be used for the PADs of SO^-, instead a multi-center and point dipole-field approach was needed to fully model the PADs. Through the investigation of SO^-, further advancements in the dipole-field model were made by introducing the detachments from the π^* orbitals.

In Chapter 4, the experimental photoelectron energy spectrum of hot phenide anion was analyzed using statistical methods as the usual *ab initio* approach, commonly used for cold anions only, proved impractical for a thermally excited polyatomic ensemble. Several models were proposed and attempted to analyze the broad and congested energy spectrum. One of the models,

the energy conservation model yielded the temperature for phenide at ~700 K, which was consistent to the experimental data. Overall, the high temperature polyatomic ions produce congested spectra due to the high density of states making state-specific approaches unrealistic to use. The use of statistical models, such as the energy conservation model, allows an efficient mean to analyze these spectra.

Chapter 5 introduced the idea of microhydration on hot ions (i.e., hot phenide-water clusters). Again, *ab initio* calculations could not be used due to their impracticality for hot ions; therefore, statistical methods helped analyze and explain the microhydration interactions involving hot phenide. The calculated ensemble average showed how the calculated harmonic limit and classical limit breaks down at high temperatures for polyatomic ensembles. Using the energy conservation model, the characteristic solvation temperature for $Ph^{-}H_2O$ and $Ph^{-}(H_2O)_2$ was determined to be around 560 K and 520 K, respectively.

The rest of this chapter will include several future directions of this research, including some preliminary results on O_2^- Benzoxazole. As hot ions are a new topic in the Sanov lab, I hope to dive deeper into this subject as many reactions occur at high temperatures.

6.2 Future Directions

The experimental photoelectron angular distribution of S_2^- has been reported, but the computational PADs did not align well with the experimental PADs of S_2^-.[80] Future experiments will be conducted to first replicate the PADs of S_2^- and investigate different methods to model the PADs of S_2^-. Furthermore, $S_2^-(H_2O)_n$ studies will be conducted to understand how different anion cores are affected by the stabilization of water (e.g., S_2^- vs. O_2^-). In addition, future experiments will involve the use of both electron gun and electron cannon. With the electron cannon, hot ions

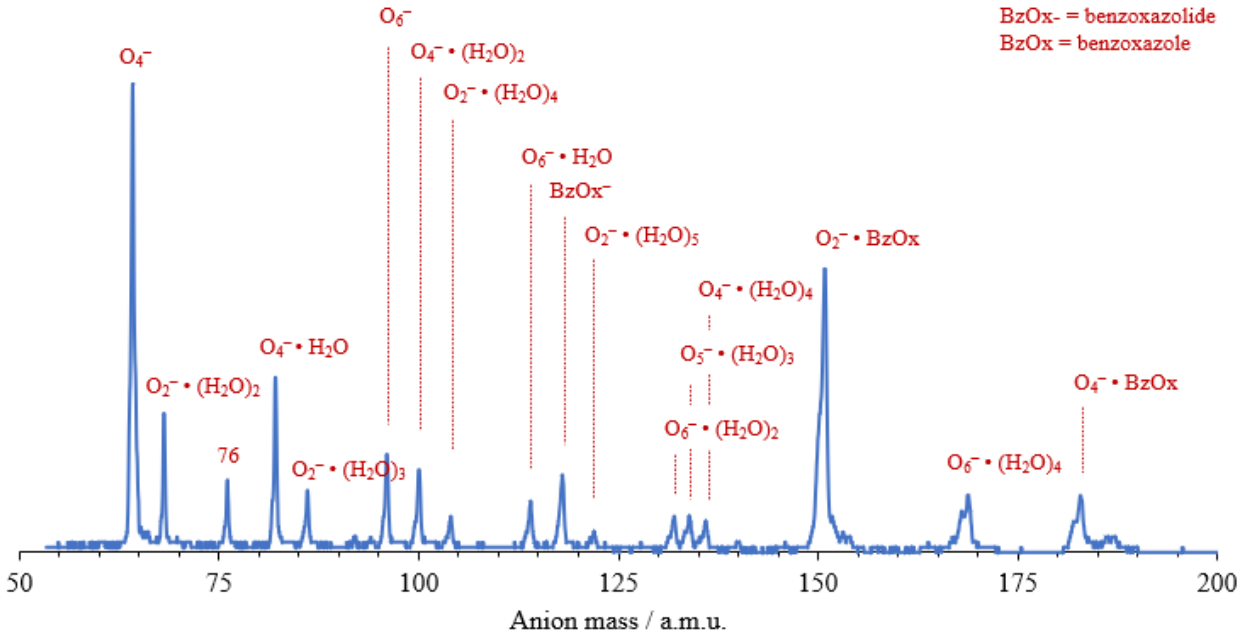

Figure 6.1: Mass spectrum of benzoxazole with O_2 carrier gas. O_2^- Bzox is at 151 amu, O_4^- Bzox at 183 amu, and benzoxazolide at 118 amu.

would be present and more likely to occur than using the electron gun. The electron gun would provide cooler temperature ions.

6.3 Preliminary Data: O_2^- Benzoxazole

O_2^- Benzoxazole extends the studies of exit-channel interactions with the neutral residue, but with the focus on the solvent molecule instead of the neutral (e.g., SO). In SO (Chapter 3), we saw how important to consider dipole moment interactions. The common assumptions of the departing electron being negligible cannot be assumed in this case as well. What differs is that the resonance states of benzoxazole are accessed. This is still being currently investigated, but some preliminary data can be addressed.

6.3.1 Experimental Methods on O_2^- Benzoxazole

O_2^- Benzoxazole was produced using benzoxazole (C_7H_5NO abbrev. Bzox) with O_2 as the carrier gas at the backing pressure of ~1.36 atm. The electron cannon (described in Section 2.6) set-up was used for this experiment and intersected the supersonic nozzle General Valve, Inc., Series 9). Negative ions were extrapolated from the plasma source using a negative repeller plate into the Wiley-McLauren TOF mass spectrometer (Section 2.3).[13] The mass spectrum obtained is shown in Figure 6.1. Ions (O_2^- Bzox, O_4^- Bzox, and benzoxazolide) were intersected by a pulsed laser beam. A Spectra Physics Lab- 130-50 Nd:YAG laser (repetition rate of 50 Hz) was used to produce the 532 nm and 355 nm using the second and third harmonic, respectively. These laser specifications were described more in Section 2.4. Photoejected electrons were projected using a VMI assembly (Section 2.5). Photoelectron images were obtained *via* inverse Abel transformation and the BASEX program.[16-17]

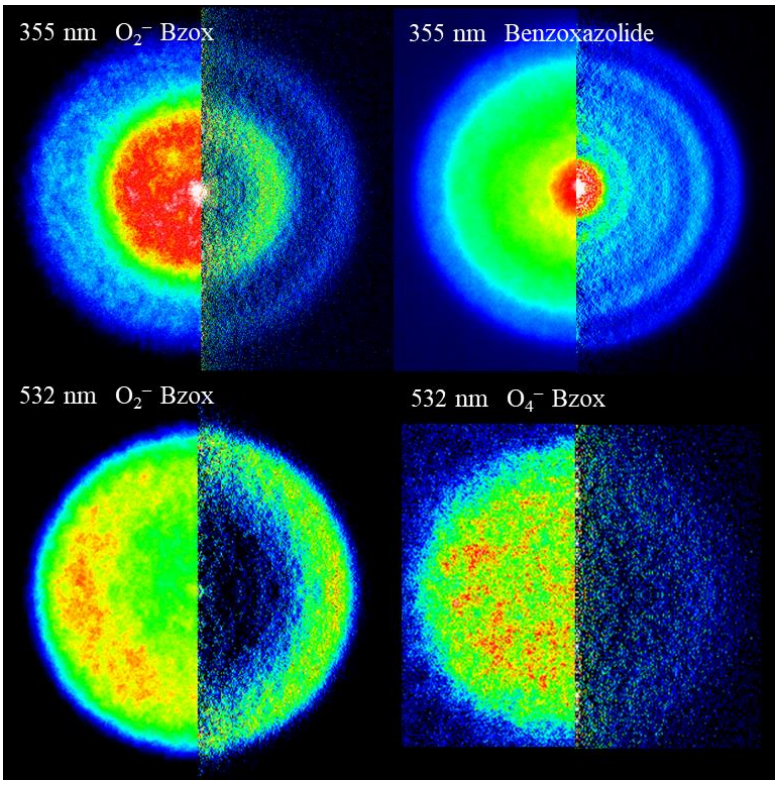

Figure 6.2: Photoelectron images of O_2^- Benzoxazole. The left half of each image is the raw photoelectron image, and the right half represented the inverse Abel transformation. O_2^- Bzox was imaged at 355 nm and 532 nm. O_4^- Bzox was imaged at 532 nm and benzoxazolide was imaged at 355 nm.

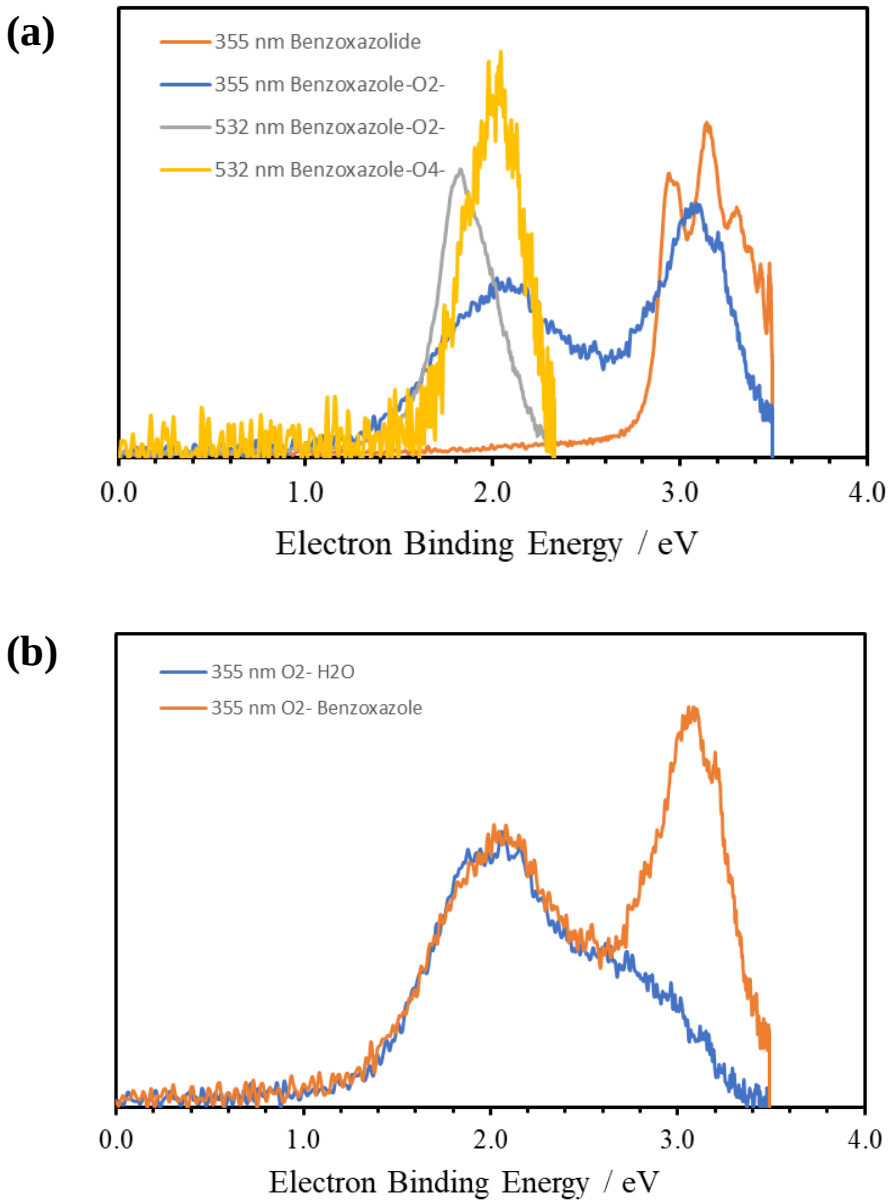

Figure 6.3: Photoelectron spectrum of O_2^- Benzoxazole. (a) This energy spectrum corresponds to the photoelectron images shown in Figure 6.2. (b) O_2^- Benzoxazole is compared to O_2^- H_2O. The intense peak on O_2^- Bzox compared to O_2^- H_2O possibly represents the resonance states of bzox. This is currently being investigated.

Benzoxazole (A″)	Method	Basis	Energy (eV)
CAP(0)	EOM-CCSD	aug-cc-pVDZ	0.9131
CAP(1)	EOM-CCSD	aug-cc-pVDZ	0.9121
CAP(0)	EOM-CCSD	aug-cc-pVDZ+1s1p1d	0.9054
CAP(1)	EOM-CCSD	aug-cc-pVDZ+1s1p1d	0.8907
CAP(0)	EOM-CCSD	aug-cc-pVDZ+2s2p2d	0.9013
CAP(1)	EOM-CCSD	aug-cc-pVDZ+2s2p2d	0.8888

Table 6.1: Benzoxazole A″ energy calculations applying CAP method. The method and basis sets used was EOM-CCSD/aug-cc-pVDZ+XsXpXd with X = 0, 1, 2.

6.3.2 Experimental Results and Analysis on O_2^- Benzoxazole

O_2^- Bzox was imaged at 355 nm and 532 nm. In addition, O_4^- Bzox and benzoxazolide was imaged at 532 nm and 355 nm, respectively. These photoelectron images can be seen in Figure 6.2. The left half of each image is the raw photoelectron image, and the right half is the inverse Abel photoelectron image. The energy spectrum of all four images can be seen in (a) of Figure 6.3, while (b) in this figure shows the comparison between O_2^- Bzox and O_2^- H_2O. What is noticed right away is that the intense right peak of the O_2^- Bzox spectrum compared to O_2^- H_2O. This is currently being investigated with the current assumption that resonance states of benzoxazole are being accessed.

6.3.3 Computational Data on Benzoxazole

Computational calculations on benzoxazole have been on going at CCSD level of theory. Geometry optimization on benzoxazole was done at method/basis of CCSD/aug-cc-pVDZ. There are two irreducible representations for the C_s symmetry: A′ and A″. Complex absorbing potential (CAP) is being applied with the EOM-EA-CCSD method to benzoxazole to understand these resonance states using Q-Chem 5.1.[81-83] Single point energy calculations on A′ and A″ were done at EOM-CCSD/6-31+G* with their energies at -398.4949 and -398.5075 Hartree, respectively to determine which was the lower lying state. Other basis set, aug-cc-pVDZ, along with diffuse functions can be seen in Table 6.1 for A″ state. Diffuse functions added to the basis sets were done like Chapter 3 diffuse functions on SO^-. Note that all experimental data and theoretical calculations are still being understood and analyzed.

Appendix – MATLAB Analysis and Codes

A.1 Finding Anisotropy Parameters

The file name for finding beta anisotropy parameters is "BetaCalculation.m". This code, written in MATLAB, is used to calculate the beta anisotropy parameter for each peak for a given range in the energy spectrum. The user-friendly program is filled with comments and descriptions of what each code block will perform. The variables are named specifically for what they are used for or contain information about. The two input files needed for this are the speed.dat and polar.dat files which are obtained from the program BASEX. The outputs list the beta parameters for the user-specific peak.

Start of code.

```
clear;clc;close all;clear all;
%% INTRODUCTION
%  Author: Beverly Feng
%  Last Edited: April 20, 2023
%  Description: This program will calculate the beta anisotropy parameter
%               in each peak for a given range.
%  Files needed in directory: 1. speed.dat
%                             2. polar.dat

%% OBTAIN DIRECTORY AND FIND POLAR.DAT FILES
%  Print all directories and obtain user input
%  Find all files with the extensions of polar.dat in the directory
files = dir;
directories = [files.isdir];
folders = files(directories);
numFigures = 1;
for index = 1:length(folders)
    fprintf('%d. %s\n',index,folders(index).name);
end

userInput = input('Enter directory number (above): ');
userFile = dir(folders(userInput).name);
fileArray = {};
for index = 1:length(userFile)
    if contains(userFile(index).name,'polar.dat')
        fileArray = [fileArray,[folders(userInput).name,'/',userFile(index).name]];
    end
end

%% PLOT SPEED.DAT AND I(THETA), OBTAIN RADIUS RANGE, CALCULATE BETA
%  Plot the speed.dat file corresponding to the polar.dat file
```

```
for i = 1:length(fileArray)
    currentFile = char(fileArray(i));
    polarFile = load(currentFile);
    speedFile = [currentFile(1:length(currentFile)-9),'speed.dat'];
    speedFile = load(speedFile);

    figure(numFigures);
    numFigures = numFigures+1;
    plot(speedFile(:,1),speedFile(:,2));
    title('speed.dat: Intensity vs. Radius'); xlabel('Radius'); ylabel('Intensity
(arb. units)');

    % Find number of peaks and their lower and upper boundaries
    fprintf('\nUsing %s\n',char(fileArray(i)));
    numPeaks = input('Enter number of peaks: ');
    peakRange = zeros(numPeaks,2);

    % Intensity(theta) calculation
    intensityTheta = zeros(160,2);
    for indexRange = 1:numPeaks
        fprintf('PEAK %d\n',indexRange);
        peakRange(indexRange,1) = input('     Enter lower radius boundary (whole
number): ');
        peakRange(indexRange,2) = input('     Enter upper radius boundary (whole
number): ');
        startIndex = find(peakRange(indexRange,1) == polarFile(:,1), 1,'first');
        endIndex = find(peakRange(indexRange,2) == polarFile(:,1), 1,'last');
        polarFileFilter = polarFile(startIndex:endIndex,:);
        unsorted = [polarFileFilter(:,2),polarFileFilter(:,1),polarFileFilter(:,3)];
        sorted = sortrows(unsorted);
        indexCurve = 1;
        indexTheta = 1;

        while (indexTheta <= length(sorted))
            startIndex = find(sorted(indexTheta,1) == sorted(:,1),1,'first');
            endIndex = find(sorted(indexTheta,1) == sorted(:,1),1,'last');
            intensityTheta(indexCurve,1) = sorted(indexTheta,1);
            intensityTheta(indexCurve,2) =
sum(sorted(startIndex:endIndex,3).*sorted(startIndex:endIndex,2));
            indexCurve = indexCurve+1;
            indexTheta = endIndex+1;
        end

        % Fitting and plotting I(theta)
        ft = fittype('a*(1+beta/2*(3*cos(x*pi/180)^2-
1))','independent','x','dependent','y');
        fitOptions = fitoptions(ft);
        fitOptions.Lower = [-Inf -Inf]; fitOptions.Upper = [Inf Inf];
        fitOptions.StartPoint = [0.970592781760616 0.957166948242946];
        [fitresult, gof] =
fit(intensityTheta(:,1),intensityTheta(:,2),ft,fitOptions);
        beta = coeffvalues(fitresult);
        fprintf('     Beta value for peak %d is %f\n',indexRange,beta(1,2));
        disp(fitresult);
        figure(numFigures);
```

```
        numFigures = numFigures+1;
        plot(fitresult,intensityTheta(:,1),intensityTheta(:,2));
        title('Intensity vs. Theta'); xlabel('Theta (degrees)'); ylabel('Intensity
(arb. units)');
    end
end
```

End of code.

A.2 Understanding Hot O_2^-

This MATLAB code was written to understand the differences between cold and hot O_2^-. The experimental O_2^- appeared to be hot and appeared to have different vibrational intensities when compared to the cold spectrum of O_2^-. This program allows the different state (ground and first two excited states) intensities to be adjusted by changing the ratio of how much each state contributes to the hot spectrum. This program calls for functions created by Dr. Sanov not listed in this block of code.

Start of code.

```
clc; clearvars;

%% Files %%
% Load files and puts it in a cell format
FCF = struct2cell(load('FCF_O2_X1_6.mat'));
FCF = [FCF,struct2cell(load('FCF_O2_a1_6.mat'))];
FCF = [FCF,struct2cell(load('FCF_O2_b1_6.mat'))];

%% Parameters %%
nF = length(FCF); % num of Files
Lambda = 355;
kT = 500;
w = 0.039;
nW = 0;
Pw1 = 1.5;
Pw2 = 2.5;
Pw3 = 3.5;
Display_coeff = 0.99;

% For 3 files (Varying intensities of FCF)
f1 = 1;
f2 = 1.8;
f3 = 2;

keep = 0;
```

```
linecolor = [0.0,0.5,1]; % green [0.06,0.6,0.4];  blue = [0.0,0.5,1]


%% Main %%
% Variables %
kT = kT/11605;   % K -> eV conversion
kTref = 1/11605;
xmin = 0;
xmax = 3.6;
npoints = 1000;
stepsize = (xmax-xmin)/(npoints-1);
broad = zeros(npoints,nF);
fx = zeros(npoints,nF);
ffcon_x = zeros(npoints,nF);

% % Changing FCF intensities
% for i = 1:nF
%     temp = FCF{1,i};
%     if i == 1
%         temp(:,2) = temp(:,2)*f1;
%     elseif i == 2
%         temp(:,2) = temp(:,2)*f2;
%     elseif i == 3
%         temp(:,2) = temp(:,2)*f3;
%     end
%
%     FCF{1,i} = temp;
% end

% Converts EA to units of K to eV
for i = 1:nF
    temp = FCF{1,i};
    temp(:,3) = temp(:,3)*kTref;
    FCF{1,i} = temp;
end

% Calculation
for i = 1:nF
    temp = FCF{1,i};
    nsticks = length(temp);
    StickX = zeros(nsticks,2);
    for j = 1:nsticks
        Ean = temp(j,3);
        if Ean < 2.495
            StickX(j,1) = temp(j,1);
            eBE = StickX(j,1);
            if i == 1
                StickX(j,2) = ((temp(j,2))^2)*exp(-Ean/kT);
            elseif i == 2
                StickX(j,2) = ((temp(j,2))^2)*exp(-Ean/kT);
            elseif i == 3
                StickX(j,2) = ((temp(j,2))^2)*exp(-Ean/kT);
            end
            %StickX(j,2) = (temp(j,2)^2)*exp(-Ean/kT);
        end
```

```
    end
    FCF{2,i} = StickX; % StickX (Ean,FCF)
    FCF{3,i} = FC_conv5(StickX,0.002); % BandX
end

% More calculations...
for i = 1:nF
    temp = FCF{3,i}; % BandX
    for j = 1:npoints
        x(j) = xmin+stepsize*(j-1);
        fx(:,i) = temp;
        fb(j) = O2_355(x(j));
    end
end

if Lambda==355
    fb = Display_coeff(3*nW+1)*fb/max(fb);
elseif Lambda==532
    fb = Display_coeff(3*nW+2)*fb/max(fb);
elseif Lambda==611
    fb = Display_coeff(3*nW+3)*fb/max(fb);
end

fcombined = f1*fx(:,1) + f2*fx(:,2) + f3*fx(:,3);


% Multiply by Wigner function
for i = 1:npoints
        eKE(i) = (6.626E-34)*(3.0E8)/(Lambda*1.0E-9*1.602E-19)-x(i);
        if eKE(i) < 0
            eKE(i) = 0;
        end
        fcombined(i) = fcombined(i)*((eKE(i))^Pw1+(2*(eKE(i))^Pw2)+(eKE(i))^Pw3);

end

% More calculations...
for i = 1:npoints
        w1 = w*eKE(i)^0.5;
        if w1==0
            w1 = w*((xmax-xmin)/(npoints-1))^0.5;
        end
        for k = 1:npoints
            broad(k) = (1/w1)*exp(-0.5*((x(k)-0.5*xmax)/w1)^2);

            if ((i-k+0.5*npoints)>0)&&((i-k+0.5*npoints)<=npoints)
               ffcon_x(i) = ffcon_x(i)+fcombined(i-k+0.5*npoints)*broad(k);
            end
        end
end

% More calculations...
fb = fb/max(fb);
fconv = ffcon_x/sum(ffcon_x);
fconv = Display_coeff*fconv/max(fconv);
```

```
% Figure
figure(Lambda+nW);
set(gcf,'position',[60,122,738,445]);

if nW == 0
%    plot(x,fx,':','LineWidth',0.6);
%    hold on
    plot(x,fb,':k','LineWidth',1.6);
    hold on
%    plot(x,fcombined,'-b','LineWidth',0.6);
%    hold on
   plot(x,fconv,'-r','LineWidth',2);

end

hold off
xlim([0.0 3.6]);
hold on
plot([0 100],[0 0],'-k');
hold off

set(gca,'XMinorTick','on','YMinorTick','off','YTick',[],'box','off',...
    'XAxisLocation','bottom');
set(gca,'XTickLabel',num2str(get(gca,'XTick')','%.1f'));

set(gca,'FontSize',18);
set(gca,'FontName','Times New Roman');
ax = gca;
ax.YAxis.Visible = 'off';
xax = ax.XAxis;
set(xax,'TickDirection','out');
ax.TickLength = [0.018, 0.012];
ax.LineWidth = 1.0;
drawnow
```

End of code.

References

1. Lohmann, U.; Feichter, J., Global indirect aerosol effects: a review. *Atmos. Chem. Phys.* **2005,** *5* (3), 715-737.

2. Yu, F.; Turco, R. P., Ultrafine aerosol formation via ion-mediated nucleation. *Geophys. Res. Lett.* **2000,** *27*, 883 - 886.

3. Sanov, A., Laboratory-Frame Photoelectron Angular Distributions in Anion Photodetachment: Insight into Electronic Structure and Intermolecular Interactions. *Annu. Rev. Phys. Chem.* **2014,** *65*, 341-363.

4. Cooper, J.; Zare, R. N., Angular Distributions in Atomic Anion Photodetachment. *J. Chem. Phys.* **1968,** *48*, 942-943.

5. Cooper, J.; Zare, R. N., Angular Distributions in Atomic Anion Photodetachment (Erratum). *J. Chem. Phys.* **1968,** *49*, 4252.

6. Cooper, J.; Zare, R. N., Photoelectron angular distributions. In *Atomic collision processes*, Geltman, S.; Mahanthappa, K. T.; Brittin, W. E., Eds. Gordon and Breach, Science Publishers: New York, London, Paris, 1968; Vol. XI-C, pp 317-337.

7. Bethe, H. A.; Salpeter, E. E., *Quantum Mechanics of One- and Two-Electron Atoms*. Springer-Verlag; Academic Press Inc.: Berlin; New York, 1957.

8. Khuseynov, D.; Blackstone, C. C.; Culberson, L. M.; Sanov, A., Photoelectron angular distributions for states of any mixed character: An experiment-friendly model for atomic, molecular, and cluster anions. *J. Chem. Phys.* **2014,** *141* (12), 124312.

9. Hanstorp, D.; Bengtsson, C.; Larson, D. J., Angular distributions in photodetachment from O^-. *Phys. Rev. A* **1989,** *40* (2), 670-675.

10. Culberson, L. M. Molecular Electronic Structure via Photoelectron Imaging Spectroscopy. Ph.D. dissertation, University of Arizona, Tucson, 2013.

11. Mabbs, R.; Surber, E.; Sanov, A., Photoelectron Imaging of Negative Ions: Atomic Anions to Molecular Clusters. *Analyst* **2003,** *128* (6), 765-772.

12. Blackstone, C. C. Exploring the Chemisty of Methoxide with Oxygen Through Photoelectron Imaging Spectroscopy. University of Arizona, Tucson, 2020.

13. Wiley, W. C.; McLaren, I. H., Time-of-Flight Mass Spectrometer with Improved Resolution. *Rev. Sci. Instrum.* **1955,** *26* (12), 1150.

14. Johnson, M. A.; Alexander, M. L.; Lineberger, W. C., Photodestruction cross sections for mass-selected ion clusters: $(CO_2)_n^+$. *Chem. Phys. Lett.* **1984,** *112* (4), 285-290.

15. Pichugin, K. Electronic Structure and Reaction Dynamics of Molecular and Cluster Anions via Photoelectron Imaging. Ph.D. dissertation, University of Arizona, 2010.

16. Dribinski, V.; Ossadtchi, A.; Mandelshtam, V. A.; Reisler, H., Reconstruction of abel-transformable images: The Gaussian basis-set expansion abel transform method. *Rev. Sci. Instrum.* **2002,** *73* (7), 2634-2642.

17. Heck, A. J. R.; Chandler, D. W., Imaging Techniques For the Study of Chemical Reaction Dynamics. *Annu. Rev. Phys. Chem.* **1995,** *46*, 335-372.

18. Ru, B.; Hart, C. A.; Mabbs, R.; Gozem, S.; Krylov, A. I.; Sanov, A., Dipole effects in the photoelectron angular distributions of the sulfur monoxide anion. *Phys. Chem. Chem. Phys.* **2022,** *24* (38), 23367-23381.

19. Shao, Y. H.; Gan, Z. T.; Epifanovsky, E.; Gilbert, A. T. B.; Wormit, M.; Kussmann, J.; Lange, A. W.; Behn, A.; Deng, J.; Feng, X. T.; Ghosh, D.; Goldey, M.; Horn, P. R.; Jacobson, L. D.; Kaliman, I.; Khaliullin, R. Z.; Kus, T.; Landau, A.; Liu, J.; Proynov, E. I.; Rhee, Y. M.;

Richard, R. M.; Rohrdanz, M. A.; Steele, R. P.; Sundstrom, E. J.; Woodcock, H. L.; Zimmerman, P. M.; Zuev, D.; Albrecht, B.; Alguire, E.; Austin, B.; Beran, G. J. O.; Bernard, Y. A.; Berquist, E.; Brandhorst, K.; Bravaya, K. B.; Brown, S. T.; Casanova, D.; Chang, C. M.; Chen, Y. Q.; Chien, S. H.; Closser, K. D.; Crittenden, D. L.; Diedenhofen, M.; DiStasio, R. A.; Do, H.; Dutoi, A. D.; Edgar, R. G.; Fatehi, S.; Fusti-Molnar, L.; Ghysels, A.; Golubeva-Zadorozhnaya, A.; Gomes, J.; Hanson-Heine, M. W. D.; Harbach, P. H. P.; Hauser, A. W.; Hohenstein, E. G.; Holden, Z. C.; Jagau, T. C.; Ji, H. J.; Kaduk, B.; Khistyaev, K.; Kim, J.; Kim, J.; King, R. A.; Klunzinger, P.; Kosenkov, D.; Kowalczyk, T.; Krauter, C. M.; Lao, K. U.; Laurent, A. D.; Lawler, K. V.; Levchenko, S. V.; Lin, C. Y.; Liu, F.; Livshits, E.; Lochan, R. C.; Luenser, A.; Manohar, P.; Manzer, S. F.; Mao, S. P.; Mardirossian, N.; Marenich, A. V.; Maurer, S. A.; Mayhall, N. J.; Neuscamman, E.; Oana, C. M.; Olivares-Amaya, R.; O'Neill, D. P.; Parkhill, J. A.; Perrine, T. M.; Peverati, R.; Prociuk, A.; Rehn, D. R.; Rosta, E.; Russ, N. J.; Sharada, S. M.; Sharma, S.; Small, D. W.; Sodt, A.; Stein, T.; Stuck, D.; Su, Y. C.; Thom, A. J. W.; Tsuchimochi, T.; Vanovschi, V.; Vogt, L.; Vydrov, O.; Wang, T.; Watson, M. A.; Wenzel, J.; White, A.; Williams, C. F.; Yang, J.; Yeganeh, S.; Yost, S. R.; You, Z. Q.; Zhang, I. Y.; Zhang, X.; Zhao, Y.; Brooks, B. R.; Chan, G. K. L.; Chipman, D. M.; Cramer, C. J.; Goddard, W. A.; Gordon, M. S.; Hehre, W. J.; Klamt, A.; Schaefer, H. F.; Schmidt, M. W.; Sherrill, C. D.; Truhlar, D. G.; Warshel, A.; Xu, X.; Aspuru-Guzik, A.; Baer, R.; Bell, A. T.; Besley, N. A.; Chai, J. D.; Dreuw, A.; Dunietz, B. D.; Furlani, T. R.; Gwaltney, S. R.; Hsu, C. P.; Jung, Y. S.; Kong, J.; Lambrecht, D. S.; Liang, W. Z.; Ochsenfeld, C.; Rassolov, V. A.; Slipchenko, L. V.; Subotnik, J. E.; Van Voorhis, T.; Herbert, J. M.; Krylov, A. I.; Gill, P. M. W.; Head-Gordon, M., Advances in molecular quantum chemistry contained in the Q-Chem 4 program package. *Mol. Phys.* **2015,** *113* (2), 184-215.

20. Gozem, S.; Krylov, A. I., The ezSpectra suite: An easy-to-use toolkit for spectroscopy modeling. *Wiley Interdiscip. Rev.: Comput. Mol. Sci.* **2021,** *12* (2), e1546.

21. Hart, C. A.; Lyle, J.; Spellberg, J.; Krylov, A. I.; Mabbs, R., Role of the Electron–Dipole Interaction in Photodetachment Angular Distributions. *J. Phys. Chem. Lett.* **2021,** *12* (41), 10086-10092.

22. Wu, F.; Chen, X. R.; Weiner, B. R., The photochemistry of ethylene episulfoxide. *J. Am. Chem. Soc.* **1996,** *118* (35), 8417-8424.

23. Ono, S., Photochemistry of Sulfur Dioxide and the Origin of Mass-Independent Isotope Fractionation in Earth's Atmosphere. *Annu. Rev. Earth Planet. Sci.* **2017,** *45* (1), 301-329.

24. Storelvmo, T., Aerosol Effects on Climate via Mixed-Phase and Ice Clouds. *Annu. Rev. Earth Planet. Sci.* **2017,** *45* (1), 199-222.

25. Ward, P. L., Sulfur dioxide initiates global climate change in four ways. *Thin Solid Films* **2009,** *517* (11), 3188-3203.

26. Russell, C. T.; Kivelson, M. G., Evidence for sulfur dioxide, sulfur monoxide, and hydrogen sulfide in the Io exosphere. *J. Geophys. Res.* **2001,** *106*, 33267-33272.

27. Turner, B. E., Interstellar SO +. *Astrophys. J.* **1994,** *430*, 727.

28. Clark, W. W.; De Lucia, F. C., The microwave spectrum and rotational structure of the 1Δ and 3Σ electronic states of sulfur monoxide. *J. Mol. Spectrosc.* **1976,** *60* (1), 332-342.

29. Jursic, B. S., Theoretical study of the atomization energy and geometry of sulfur dioxide and sulfur monoxide. *J. Mol. Struct.* **1999,** *467* (3), 187-193.

30. Bogey, M.; Civiš, S.; Delcroix, B.; Demuynck, C.; Krupnov, A. F.; Quiguer, J.; Tretyakov, M. Y.; Walters, A., Microwave Spectrum up to 900 GHz of SO Created in Highly

Excited States by Electric Discharge and UV-Laser Photolysis. *J. Mol. Spectrosc.* **1997,** *182* (1), 85-97.

31. Polak, M. L.; Fiala, B. L.; Ervin, K. M.; Lineberger, W. C., The ultraviolet photoelectron spectrum of SO^-. *J. Chem. Phys.* **1991,** *94* (10), 6926-6927.

32. Polak, M. L.; Fiala, B. L.; Ervin, K. M.; Lineberger, W. C., The ultraviolet photoelectron spectrum of SO/sup -/. *J. Chem. Phys.* **1991,** *94* (10), 6926-7.

33. Blackstone, C. C.; Wallace, A. A.; Sanov, A., Photoelectron angular distributions in photodetachment from polarized *d*-like states: The case of HO_2^-. *Mol. Phys.* **2021,** *119*, e1831636.

34. Van Duzor, M.; Mbaiwa, F.; Wei, J.; Singh, T.; Mabbs, R.; Sanov, A.; Cavanagh, S. J.; Gibson, S. T.; Lewis, B. R.; Gascooke, J. R., Vibronic coupling in the superoxide anion: The vibrational dependence of the photoelectron angular distribution. *J. Chem. Phys.* **2010,** *133* (17), 174311.

35. Krylov, A. I., From orbitals to observables and back. *J. Chem. Phys.* **2020,** *153* (8), 080901.

36. Ortiz, J. V., Dyson-orbital concepts for description of electrons in molecules. *J. Chem. Phys.* **2020,** *153* (7), 070902.

37. Moitra, T.; Ponzi, A.; Koch, H.; Coriani, S.; Decleva, P., Accurate Description of Photoionization Dynamical Parameters. *J. Phys. Chem. Lett.* **2020,** *11* (13), 5330-5337.

38. Díaz–Tinoco, M.; Corzo, H. H.; Pawłowski, F.; Ortiz, J. V., Do Dyson Orbitals resemble canonical Hartree–Fock orbitals? *Mol. Phys.* **2019,** *117* (17), 2275-2283.

39. Krylov, A. I., Size-consistent wave functions for bond-breaking: the equation-of-motion spin-flip model. *Chem. Phys. Lett.* **2001,** *338* (4), 375-384.

40. Levchenko, S. V.; Krylov, A. I., Equation-of-motion spin-flip coupled-cluster model with single and double substitutions: Theory and application to cyclobutadiene. *J. Chem. Phys.* **2004,** *120* (1), 175-185.

41. Thomson, R.; Dalby, F. W., Experimental determination of the dipole moments of the X(2Σ+) and B(2Σ+) states of the CN molecule. *Canadian Journal of Physics* **1968,** *46* (24), 2815-2819.

42. Byfleet, C. R.; Carrington, A.; Russell, D. K., Electric dipole moments of open-shell diatomic molecules. *Mol. Phys.* **1971,** *20* (2), 271-277.

43. Jordan, K. D.; Wang, F., Theory of dipole-bound anions. *Annu. Rev. Phys. Chem.* **2003,** *54*, 367-396.

44. Greene, C.; Fano, U.; Strinati, G., General form of the quantum-defect theory. *Phys. Rev. A* **1979,** *19* (4), 1485-1509.

45. Gozem, S.; Seidel, R.; Hergenhahn, U.; Lugovoy, E.; Abel, B.; Winter, B.; Krylov, A. I.; Bradforth, S. E., Probing the Electronic Structure of Bulk Water at the Molecular Length Scale with Angle-Resolved Photoelectron Spectroscopy. *J. Phys. Chem. Lett.* **2020,** *11* (13), 5162-5170.

46. Celotta, R. J.; Bennett, R. A.; Levine, J.; Hall, J. L.; Siegel, M. W., Molecular Photodetachment Spectrometry .2. Electron Affinity of O2 and Structure of O2. *Phys. Rev. A* **1972,** *6* (2), 631-642.

47. Akin, F. A.; Schirra, L. K.; Sanov, A., Photoelectron imaging study of the effect of monohydration on O_2^- photodetachment. *J. Phys. Chem. A* **2006,** *110* (26), 8031-8036.

48. Mabbs, R.; Mbaiwa, F.; Wei, J.; Van Duzor, M.; Gibson, S. T.; Cavanagh, S. J.; Lewis, B. R., Observation of vibration-dependent electron anisotropy in O_2^- photodetachment. *Phys. Rev. A* **2010,** *82* (1), 011401.

49. Ru, B.; Sanov, A., Photoelectron Spectra of Hot Polyatomic Ions: A Statistical Treatment of Phenide. *J. Phys. Chem. A* **2022,** *126* (50), 9423-9439.

50. Franck, J.; Dymond, E. G., Elementary processes of photochemical reactions. *Trans. Faraday Soc.* **1926,** *21* (February), 536-542.

51. Condon, E. U., The Franck-Condon Principle and Related Topics. *Am. J. Phys.* **1947,** *15* (5), 365-374.

52. Condon, E., A Theory of Intensity Distribution in Band Systems. *Phys. Rev.* **1926,** *28* (6), 1182-1201.

53. Sivaranjana Reddy, V.; Venkatesan, T. S.; Mahapatra, S., Vibronic interactions in the photodetachment spectroscopy of phenide anion. *J. Chem. Phys.* **2007,** *126* (7), 074306.

54. Haynes, B. S.; Wagner, H. G., Soot formation. *Prog. Energy Combust. Sci.* **1981,** *7* (4), 229-273.

55. Frenklach, M., Reaction mechanism of soot formation in flames. *Phys. Chem. Chem. Phys.* **2002,** *4* (11), 2028-2037.

56. Shukla, B.; Susa, A.; Miyoshi, A.; Koshi, M., Role of Phenyl Radicals in the Growth of Polycyclic Aromatic Hydrocarbons. *J. Phys. Chem. A* **2008,** *112* (11), 2362-2369.

57. Millar, T. J.; Walsh, C.; Field, T. A., Negative Ions in Space. *Chem. Rev.* **2017,** *117* (3), 1765-1795.

58. Wakelam, V.; Herbst, E., Polycyclic Aromatic Hydrocarbons in Dense Cloud Chemistry. *Astrophys. J.* **2008,** *680* (1), 371-383.

59. Kaiser, R. I.; Parker, D. S. N.; Mebel, A. M., Reaction Dynamics in Astrochemistry: Low-Temperature Pathways to Polycyclic Aromatic Hydrocarbons in the Interstellar Medium. *Annu. Rev. Phys. Chem.* **2015,** *66* (1), 43-67.

60. Herbst, E., Chemistry in the Interstellar Medium. *Annu. Rev. Phys. Chem.* **1995,** *46* (1), 27-54.

61. Jones, B. M.; Zhang, F.; Kaiser, R. I.; Jamal, A.; Mebel, A. M.; Cordiner, M. A.; Charnley, S. B., Formation of benzene in the interstellar medium. *Proc. Nat. Acad. Sci.* **2011,** *108* (2), 452-457.

62. McQuarrie, D. A., *Statistical Mechanics*. University Science Books: Sausalito, California, 2000.

63. Hill, T. L., *An Introduction to Statistical Thermodynamics*. Dover Publications: New York, 2012.

64. Gilbert, R. G.; Smith, S. C., *Theory of unimolecular and recombination reactions*. Blackwell Scientific Publications: Oxford, England, 1990.

65. Gunion, R. F.; Gilles, M. K.; Polak, M. L.; Lineberger, W. C., Ultraviolet Photoelectron-Spectroscopy of the Phenide, Benzyl and Phenoxide Anions, with ab initio Calculations. *Int. J. Mass Spectrom.* **1992,** *117* (1-3), 601-620.

66. Feng, B.; Sanov, A., Microsolvation of Hot Ions: Spectroscopy and Statistical Mechanics of Phenide–Water Interactions. *J. Phys. Chem. A* **2023,** *127* (31), 6437-6446.

67. Castleman, A. W.; Bowen, K. H., Clusters: Structure, Energetics, and Dynamics of Intermediate States of Matter. *J. Phys. Chem.* **1996,** *100* (31), 12911-12944.

68. Sanov, A.; Lineberger, W. C., Cluster anions: Structure, interactions, and dynamics in the sub-nanoscale regime. *Phys. Chem. Chem. Phys.* **2004,** *6* (9), 2018-2032.

69. Sanov, A.; Nandi, S.; Lineberger, W. C., Transient solvent dynamics and incoherent control of photodissociation pathways in I_2^- cluster ions. *J. Chem. Phys.* **1998,** *108* (13), 5155-5158.

70. Kelley, J. A.; Weber, J. M.; Lisle, K. M.; Robertson, W. H.; Ayotte, P.; Johnson, M. A., The infrared predissociation spectra of $Cl^-\cdot H_2O\cdot Ar_n$ (n = 1-5): experimental determination of the influence of Ar solvent atoms. *Chem. Phys. Lett.* **2000,** *327* (1-2), 1-6.

71. Ayotte, P.; Weddle, G. H.; Kim, J.; Johnson, M. A., Mass-selected "matrix isolation" infrared spectroscopy of the $I^-\cdot(H_2O)_2$ complex: making and breaking the inter-water hydrogen-bond. *Chem. Phys.* **1998,** *239* (1), 485-491.

72. Ayotte, P.; Weddle, G. H.; Kim, J.; Johnson, M. A., Vibrational Spectroscopy of the Ionic Hydrogen Bond: Fermi Resonances and Ion−Molecule Stretching Frequencies in the Binary $X^-\cdot H_2O$ (X = Cl, Br, I) Complexes via Argon Predissociation Spectroscopy. *J. Am. Chem. Soc.* **1998,** *120* (47), 12361-12362.

73. Elliott, B. M.; Relph, R. A.; Roscioli, J. R.; Bopp, J. C.; Gardenier, G. H.; Guasco, T. L.; Johnson, M. A., Isolating the spectra of cluster ion isomers using Ar-"tag"-mediated IR-IR double resonance within the vibrational manifolds: Application to $NO_2^-\cdot H_2O$. *J. Chem. Phys.* **2008,** *129* (9), 094303.

74. Diken, E. G.; Robertson, W. H.; Johnson, M. A., The Vibrational Spectrum of the Neutral $(H_2O)_6$ Precursor to the "Magic" $(H_2O)_6^-$ Cluster Anion by Argon-Mediated, Population-Modulated Electron Attachment Spectroscopy. *J. Phys. Chem. A* **2004,** *108* (1), 64-68.

75. Wigner, E. P., On the behavior of cross sections near thresholds. *Phys. Rev.* **1948,** *73* (9), 1002-1009.

76. Simpson, M.; Nötzold, M.; Schmidt-May, A.; Michaelsen, T.; Bastian, B.; Meyer, J.; Wild, R.; Gianturco, F. A.; Milovanović, M.; Kokoouline, V.; Wester, R., Threshold photodetachment spectroscopy of the astrochemical anion CN^-. *J. Chem. Phys.* **2020,** *153* (18), 184309.

77. Engelking, P. C., Strong electron-dipole coupling in photodetachment of molecular negative ions: Anomalous rotational thresholds. *Phys. Rev. A* **1982,** *26* (2), 740-745.

78. Boys, S. F.; Bernardi, F., Calculation of Small Molecular Interactions by Differences of Separate Total Energies. Some Procedures with Reduced Errors. *Mol. Phys.* **1970,** *19* (4), 553-566.

79. Angelova, M.; Frank, A., Algebraic Model of Molecular Thermodunamics. In *Quantum Theory and Symmetries*, World Scientific: 2002; pp 243-248.

80. Surber, E.; Mabbs, R.; Sanov, A., Probing the electronic structure of small molecular anions by photoelectron imaging. *J. Phys. Chem. A* **2003,** *107*, 8215-8224.

81. Zuev, D.; Jagau, T.-C.; Bravaya, K. B.; Epifanovsky, E.; Shao, Y.; Sundstrom, E.; Head-Gordon, M.; Krylov, A. I., Complex absorbing potentials within EOM-CC family of methods: Theory, implementation, and benchmarks. *J. Chem. Phys.* **2014,** *141* (2), 024102.

82. Dauletyarov, Y.; Ru, B.; Sanov, A., Anion of Oxalyl Chloride: Structure and Spectroscopy. *J. Phys. Chem. A* **2021,** *125* (45), 9865-9876.

83. Jagau, T.-C.; Zuev, D.; Bravaya, K. B.; Epifanovsky, E.; Krylov, A. I., A Fresh Look at Resonances and Complex Absorbing Potentials: Density Matrix-Based Approach. *J. Phys. Chem. Lett.* **2014,** *5* (2), 310-315.